Identification of the

Lipid Oxygen Radical Defense pathway and its epigenetic control

Francisco S. Mesquita[1†]*, Laurence Abrami[1†], Romain Forey[1], Béatrice Kunz[1], Charlène Raclot[1], Lucie Bracq[1], Filipe Martins[1], Danica Milovanovic[1], Evarist Planet[1,2], Olga Rosspopoff[1], Didier Trono[1], and F. Gisou van der Goot[1]*

[1]Global Health Institute, School of Life Sciences, EPFL, Lausanne

[2]Nexco Analytics, Epalinges, Switzerland

†These authors contributed equally

*Corresponding Authors: F. Gisou van der Goot (gisou.vandergoot@epfl.ch), Francisco S. Mesquita (francisco.mesquita@epfl.ch)

Keywords: ZNF354A, ATF2, KAP1/TRIM28, KRAB-zinc finger protein, Oxidative stress, Lipid Peroxidation, ferroptosis, ZDHHC20, NRF2.

ABSTRACT

Membrane phospholipids are vulnerable to oxidative radicals, and uncontrolled lipid peroxidation can compromise cell viability. To mitigate lipid damage, cells have evolved defense mechanisms, the genetic regulation of which is not fully understood. Here, we identify the Lipid Oxygen Radical Defense (LORD) pathway. Under normal conditions, the pathway is epigenetically repressed by a complex comprising the KRAB-zinc finger protein ZNF354A, the scaffold protein KAP1/TRIM28, the histone methyltransferase SETDB1, and the transcriptional activator ATF2. In response to lipid peroxide accumulation, ATF2, KAP1, and ZNF354A undergo p38- and JNK-dependent phosphorylation, and the repressive complex disassembles, releasing ZNF354A from specific DNA loci. A protective gene network is subsequently activated, comprising targets of the major redox regulator NRF2 and modulating cellular sensitivity to oxidative stress and ferroptosis. These findings reveal a novel layer of epigenetic regulation in the cellular defense against lipid damage but also position the LORD pathway as a promising therapeutic target for diseases linked to chronic inflammation, neurodegeneration and cancer.

INTRODUCTION

Reactive oxygen species (ROS) are inevitable byproducts of aerobic metabolism [1,2]. These molecules play a dual role in cellular physiology: they are vital for signaling pathways [1,2], but excessive ROS accumulation leads to oxidative stress and cellular damage [1–3]. Elevated hydrogen peroxide (H_2O_2) levels can trigger Fenton reactions with transition metals, such as ferrous iron (Fe^{2+}), producing highly reactive hydroxyl radicals that inflict severe oxidative damage to biomolecules such as DNA, proteins, and lipids [1,2], particularly phospholipids containing polyunsaturated fatty acids (PUFAs) present in cellular membranes [4–6]. Accumulation of lipid peroxides and their deleterious by-products is a hallmark of oxytosis or ferroptosis, a non-apoptotic form of cell death increasingly recognized for its importance in aging, cancer, cardiovascular disease, neurodegeneration, and chronic inflammation [4,5,7–11]. Cells have evolved sophisticated antioxidant defense systems to protect against membrane lipid peroxidation, such as selenium/thiol-dependent and independent pathways [7,9,12,13]. How these protective mechanisms are regulated at a transcriptional level, particularly in complex organisms like mammals [14], is not fully understood, and is the focus of the present study.

A complex network of transcription factors responds to oxidative stress in a coordinated manner [2,9,14–16]. In the main conserved system, Keap1/NRF2 (NF-E2-related factor 2), regulates diverse antioxidant response elements that drive the expression of antioxidant genes, and xenobiotic transporters [15–18]. NRF2 enhances protection by controlling iron and specific detoxification pathways [15,17,19]. These include the thiol-independent oxidoreductase FSP1 (ferroptosis suppressor 1) [20–22] and factors required for glutathione (GSH) synthesis, such as SLC7A11 [23,24] and the cystine/glutamate antiporter crucial for cystine uptake. GSH is essential for the activity of GPX4 (glutathione peroxidase-4), the primary enzyme reducing lipid hydroperoxides [13,25], which is regulated by NRF1, suggesting overlapping functions but distinct cellular targets among transcription factors [26]. Other factors like NF-κB, HIF-1, FOXO1, p53, YAP/TAZ, and ATF4 are also involved in maintaining redox balance, influencing lipid peroxidation, inflammation, and hypoxia responses, ultimately affecting

cellular sensitivity to oxidative stress[2,14,27–31]. Redox-driven epigenetic modifications can further shape the expression of specific antioxidant genes [32–34]. However, despite this wealth of information, major gaps in understanding the transcriptional regulation of lipid peroxidation defenses remain. The existence of a master regulator remains uncertain, and the mechanisms triggering specific antioxidant gene programs under stress conditions are yet to be elucidated.

In this study, we uncover an epigenetically regulated defense pathway against ROS-triggered lipid damage, which we have termed the LORD pathway, for Lipid Oxygen Radical Defense. This pathway is under epigenetic regulation. The master regulator is ZNF354A, a member of the largest family of mammalian transcriptional modulators, the Krüppel-associated box (KRAB) domain zinc finger protein (KZFP) [35,36]. ZNF354A is part of a non-canonical repressive complex containing the global repressor KAP1 (TRIM28), the histone methyltransferase SETDB1, but also the transcriptional activator ATF2. Under homeostatic conditions, ZNF354A represses transcriptional programs involved in antioxidant defenses and other response pathways. Accumulation of lipid peroxides leads to phosphorylation-dependent disassembly of the repressive complex, and release of ZNF354A from specific DNA loci, allowing activation of the lipid damage response pathway. This work highlights the underexplored dynamics of epigenetic repressive complexes and the genetic response to oxidative lipid damage. It also paves the way towards the identification of potential targets for therapeutic intervention in a variety of conditions such as chronic inflammation, infections, cancer, and aging-related disorders.

RESULTS

ZDHHC20L as a readout for the LORD pathway

In previous work on the S-acylation of the SARS-CoV-2 Spike protein by the acyltransferase ZDHHC20 [37,38], we found that infection induces a transcriptional shift in the *ZDHHC20* gene, generating N-terminally extended isoforms of the protein, which we collectively term ZDHHC20L. These longer isoforms are also expressed *in vivo*, upon chemical-induced colitis, and in cells exposed to the pore-forming toxin aerolysin[37]. We additionally documented the presence of ZDHHC20L in untreated hepatocellular carcinoma cell line HepG2 [37], a finding we extended here to MCF7 breast cancer and HCT116 human colorectal carcinoma cells (Fig. 1A). We also investigated whether ZDHHC20L expression could be induced by aging, a process where increased stress pathways are linked to the gradual decline of repair mechanisms[39]. While in total cell extracts from primary lung epithelial cells of young donors only the canonical form of ZDHHC20 was detected (Fig 1B), ZDHHC20L became increasingly expressed in cells from donors above 60 (Fig. 1B). ZDHHC20L expression is thus induced under a variety of conditions, ranging from some cancers to aging, viral infection, and other stresses. This study aimed to identify the pathway that leads to ZDHHC20L expression. While ZDHHC20L expression has interesting functional consequences, particularly in controlling cellular sensitivity to ferroptosis[40] (see discussion), it was primarily used in this study as a useful proxy for the LORD pathway.

Activation of the transcription factor ATF2 triggers ZDHHC20L expression

To elucidate the molecular mechanisms underlying ZDHHC20L expression, we mined experimental gene occupancy data of ENCODE-3 (Encyclopedia of DNA Elements) [41,42] hosted in the UCSC Genome Browser (Transcription Factor ChIP-seq Clusters)[43]. We previously found that ZDHHC20L is translated from upstream in-frame AUGs, part of longer transcripts. We also described FOXA1 and SP1 as transcription regulators binding approximately 5 kb upstream of the in-frame start codons, in HepG2 cells[37]. Here, we noticed that the stress-regulated transcriptional activator ATF2[44] was recruited ~5 kB further

upstream (Fig. 1C) and evaluated its role in ZDHHC20L expression. In Hela cells, where ZDHHC20L can be induced by aerolysin [37], we found that siRNA-silencing of ATF2 (Fig. S1A) significantly reduced ZDHHC20L expression (Fig. 1D).

Different kinases activate ATF2 in response to stress or growth signals[45–51] and aerolysin treatment also led to ATF2 (both endogenous and over-expressed) phosphorylation, on Thr-69, within its transactivation region[47] (Fig. 1D, S1B). The presence of multiple phospho-bands at around >55 kDa suggests phosphorylation on several residues and/or of various ATF2 isoforms[52]. ATF2 phosphorylation could be detected under all tested conditions leading to ZDHHC20L expression: in primary lung epithelial cells from older donors or subjected to SARS-CoV-2 infection (Fig S1C), in the duodenum of mice (where ZDHHC20L is constitutively expressed[37] - Fig S1D), and in the colon of mice upon chemical-induced colitis (Fig. S1E).

To assess the importance of ATF2 phosphorylation in regulating ZDHHC20L expression, we generated ATF2 phospho-site mutants, either mimicking phosphorylation by aspartic acid substitution or preventing it by alanine substitution, targeting four residues in the N-terminal activation domain Thr-52, 69, 71 and 73 [51] (to D or A - coined 4D and 4A), two in the C-terminal regulatory domain Ser-490 and 498 [45] (2D and 2A), or all six combined (6D and 6A). Using U2OS cells, which only express the canonical form of ZDHHC20, overexpression of any of the ATF2 phospho-mimetic mutants was sufficient to induce ZDHHC20L expression, in the absence of any stimulus (Fig. 1E, S1F). This process still required FOXA1 and SP1, as it was blocked by the combined depletion or pharmacological inhibition of these transcription factors with JQ1 and mithramycin respectively (Fig. S1G). Consistently, wild-type ATF2, but not ATF2-6A, when co-expressed with FOXA1 and SP1, also led to ZDHHC20L expression (Fig. 1E), which did not occur when only two of these factors were over-expressed (Fig. S1H).To explore an additional functional outcome beyond controlling expression of ZDHHC20L during stress, we investigated whether ATF2 activation is protective against exposure to aerolysin, which like other pore-forming toxins disrupts plasma membrane integrity that can lead to cell death [53,54]. Silencing ATF2 increased cell sensitivity

to aerolysin (Fig. 1F) which was rescued by expressing wild type (WT) or the phosphomimetic 6D ATF2 but not the 6A mutant (Fig. 1F). Thus, activated ATF2 drives ZDHHC20L and protects cells from membrane damage by aerolysin.

ZDHHC20L is repressed by a heterochromatin-inducing complex

We further analyzed ENCODE ChIP-seq data and identified binding sites for the protein scaffold KAP1 (KRAB domain-associated protein 1) and the histone methyltransferase SETDB1 (SET Domain Bifurcated Histone Lysine Methyltransferase 1), near the ATF2 binding regions in U2OS and K562 cells (Fig. 1C) [55,56]. These two proteins are part of a chromatin-modifying complex that mediates histone 3 lysine 9 trimethylation (H3K9m3), leading to the formation of heterochromatin[55] and transcriptional repression[55–58] (Fig. 1G, top panel). In U2OS cells, SETDB1 silencing (Fig. S1A) alone induced ZDHHC20L expression (Fig. 1H), which was suppressed by wild-type SETDB1 but not by a catalytically inactive mutant (Fig. 1I), confirming the need for its enzymatic activity. KAP1 silencing (Fig. S1A) or knockout in haploid HAP1 cells (Fig. 1J) similarly triggered ZDHHC20L expression (Fig. 1J) and the emergence of extended ZDHHC20 mRNA transcripts, as shown by qPCR (Fig. 1K)[37]. Given the involvement of SETDB1 and KAP1, we analyzed ENCODE ChIP-seq data to assess histone modifications at the ZDHHC20 locus. In U2OS cells, repressive H3K9me3 mark were detected around the SETDB1, KAP1, and ATF2 peaks (Fig. 1C). Additional H3K9me3 marks within the first intron overlapped a second SETDB1 peak, potentially reinforcing ZDHHC20L silencing. Active promoter marks, H3K27Ac and H3K4me3, flanked these repressive regions and co-localized with both the short-canonical and long ZDHHC20 transcription start sites (Fig. 1C, 1G). The enhancer mark H3K4me1 aligned with FOXA1 and SP1 ChIP-seq peaks in HepG2 cells, which constitutively express ZDHHC20L even without stimulation (Fig. 1C)[37]. Altogether, these data show that under homeostatic conditions the expression of ZDHHC20L isoforms is repressed by the heterochromatin-inducing KAP1/SETDB1 complex.

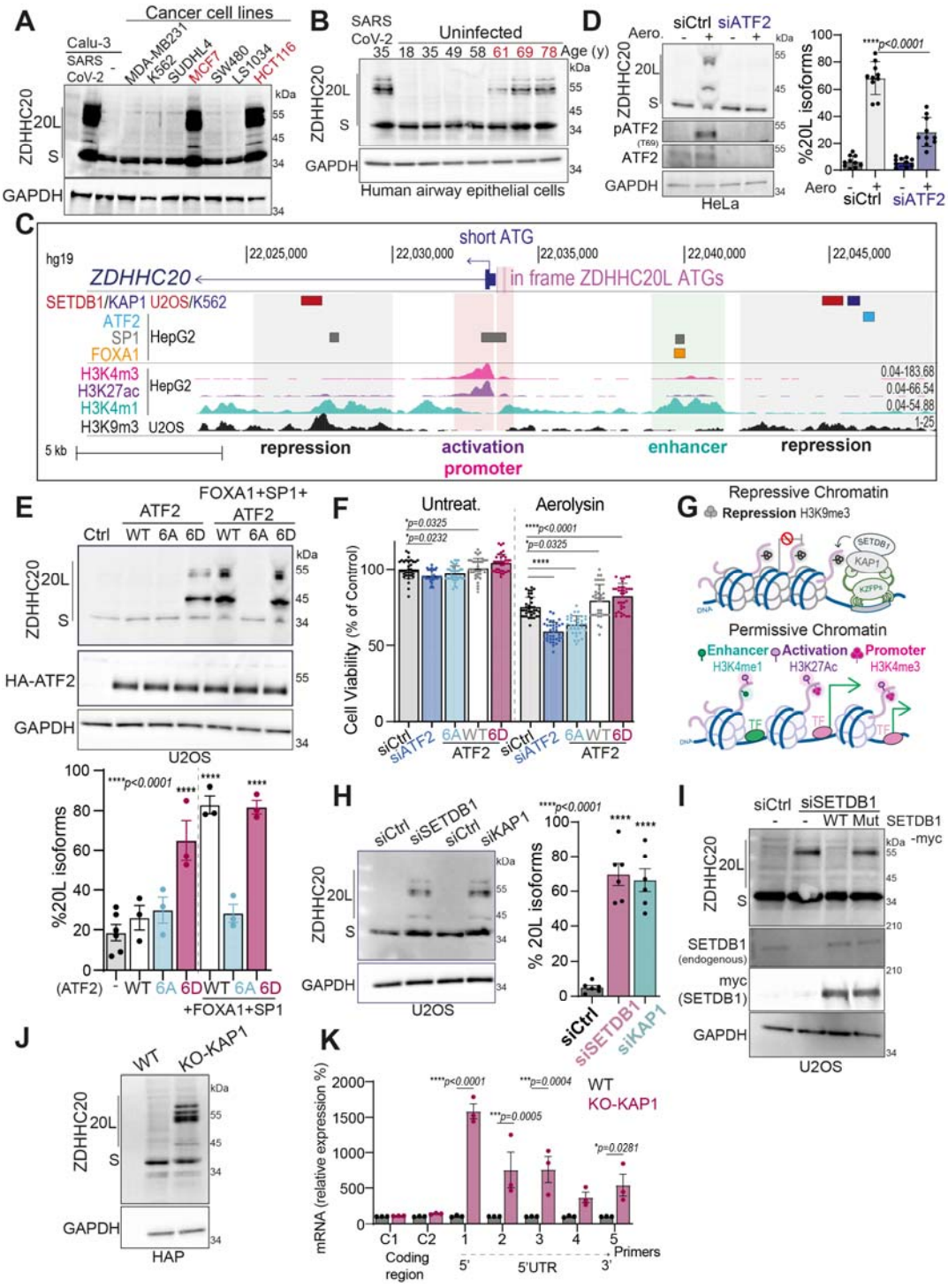
A
Cancer cell lines
Calu-3
SARS CoV-2
MDA-MB231
K562
SUDHL4
MCF7
SW480
LS1034
HCT116
ZDHHC20
20L
S
GAPDH
kDa
B
SARS CoV-2
Uninfected
35 18 35 49 58 61 69 78 Age (y)
Human airway epithelial cells
D
siCtrl siATF2
Aero.
pATF2 (T69)
ATF2
HeLa
%20L isoforms
****p<0.0001
C
hg19
short ATG
in frame ZDHHC20L ATGs
ZDHHC20
SETDB1/KAP1 U2OS/K562
ATF2
SP1
FOXA1
HepG2
H3K4m3
H3K27ac
H3K4m1
H3K9m3 U2OS
5 kb
repression
activation
promoter
enhancer
repression
E
ATF2
FOXA1+SP1+ ATF2
Ctrl WT 6A 6D WT 6A 6D
HA-ATF2
U2OS
%20L isoforms
(ATF2) - WT 6A 6D WT 6A 6D
+FOXA1+SP1
F
Untreat.
Aerolysin
Cell Viability (% of Control)
siCtrl siATF2 6A WT 6D ATF2
G
Repressive Chromatin
Repression H3K9me3
SETDB1
KAP1
KZFPs
Permissive Chromatin
Enhancer H3K4me1
Activation H3K27Ac
Promoter H3K4me3
H
siCtrl siSETDB1 siCtrl siKAP1
% 20L isoforms
I
siCtrl siSETDB1
WT Mut SETDB1 -myc
SETDB1 (endogenous)
myc (SETDB1)
J
WT KO-KAP1
HAP
K
WT
KO-KAP1
mRNA (relative expression %)
C1 C2 1 2 3 4 5 Primers
Coding region
5' 5'UTR 3'

Figure 1. ATF2 and SETDB1-KAP1 dependent induction of ZDHHC20L expression.
A-B. Western blot (WB) analysis of ZDHHC20, Short-S (42 KDa) and 20L (~49, 62 and 69 KDa), GAPDH (loading control) from lysates of: **A.** a panel of cancer cell lines and infected Calu-3 cells (SARS-CoV-2, MOI 0.1, 24 h) as comparison; **B.** primary human airway epithelia from individuals with different ages or infected with SARS-CoV-2 MOI□=□0.1, 48□h. **C.** Overview of the *ZDHHC20* locus (first intron, exon, and 5'UTR - version hg19), Tracks indicate: in-frame transcription start codons (ATGs); transcript (GENCODE-V4 0lift37); histone modifications ChIP-seq signals with minimum and maximum data points in the current view (ENCODE/Broad) - H3K9me3, black, repression; enhancer, H3K4me1 green; activation, H3K7Ac, purple; or promoter, H3K4me3, pink; SETDB1/KAP1, ATF2, SP1 and FOXA1 ChIP-seq peaks (ENCODE) **D**. WB, as (A), also showing total and phospho-ATF2 in HeLa cells siControl (siCtrl) or siATF2 left untreated or treated with 10□ng/ml of proaerolysin (toxin) for 1hr at 37□°C, washed, and incubated at 37□°C for 8 h. Correspondent quantification of 20L bands are mean□±□SEM, each dot represents one independent experiment, n□=□10; *P* values obtained by two-way ANOVA, Sidak's correction. **E.** WB as (A) in U2OS control or expressing ATF2 (WT, 6D or 6A phospho-mutants), and FOXA1 and SP1. Results are mean□±□SEM; each dot represents one independent experiment, n□=□6 (Ctrl) or n=3; *P* values compare to Ctrl, obtained by two-way ANOVA, Dunnett's correction. **F**. Cell viability, monitored by ATP detection (Promega Glo - see materials and methods), in cells treated as (E)**.** Values normalized to Untreated siCtrl, set as 100%. Results are mean ±□SD of one of three representative assays (n=34) replicates. *P* values, compared to siCtrl were obtained by two-way ANOVA, Dunnett's correction. **G.** KAP1-KZFPs recruit histone modifiers, (*e.g.* SETDB1) inducing H3K9me3-mediated chromatin repression (top), often involving removal of active marks at enhancers (H3K4me1), activation sites (H3K27Ac), and promoters (H3K4me3) (bottom) (adapted from [36]). **H.** As (D), in U2OS siCtrl, siSETDB1 or siKAP1-depleted for 72 h; Results are mean□±□SEM; each dot represents one independent experiment of n□=□6; *P* values comparing to Ctrl obtained by two-way ANOVA, Dunnett's correction. **I.** As (H), with siSETDB1 cells complemented with WT or catalytically inactive SETDB1 (Mut) for 24 h. **J**. As (A), in HAP-1 wild-type or knockout for KAP1. **K.** mRNA quantification probing different locations in Z*DHHC20* transcripts (coding region: C1, C2; 5' UTR: 1–5 cover increasing lengths of 5' ends.

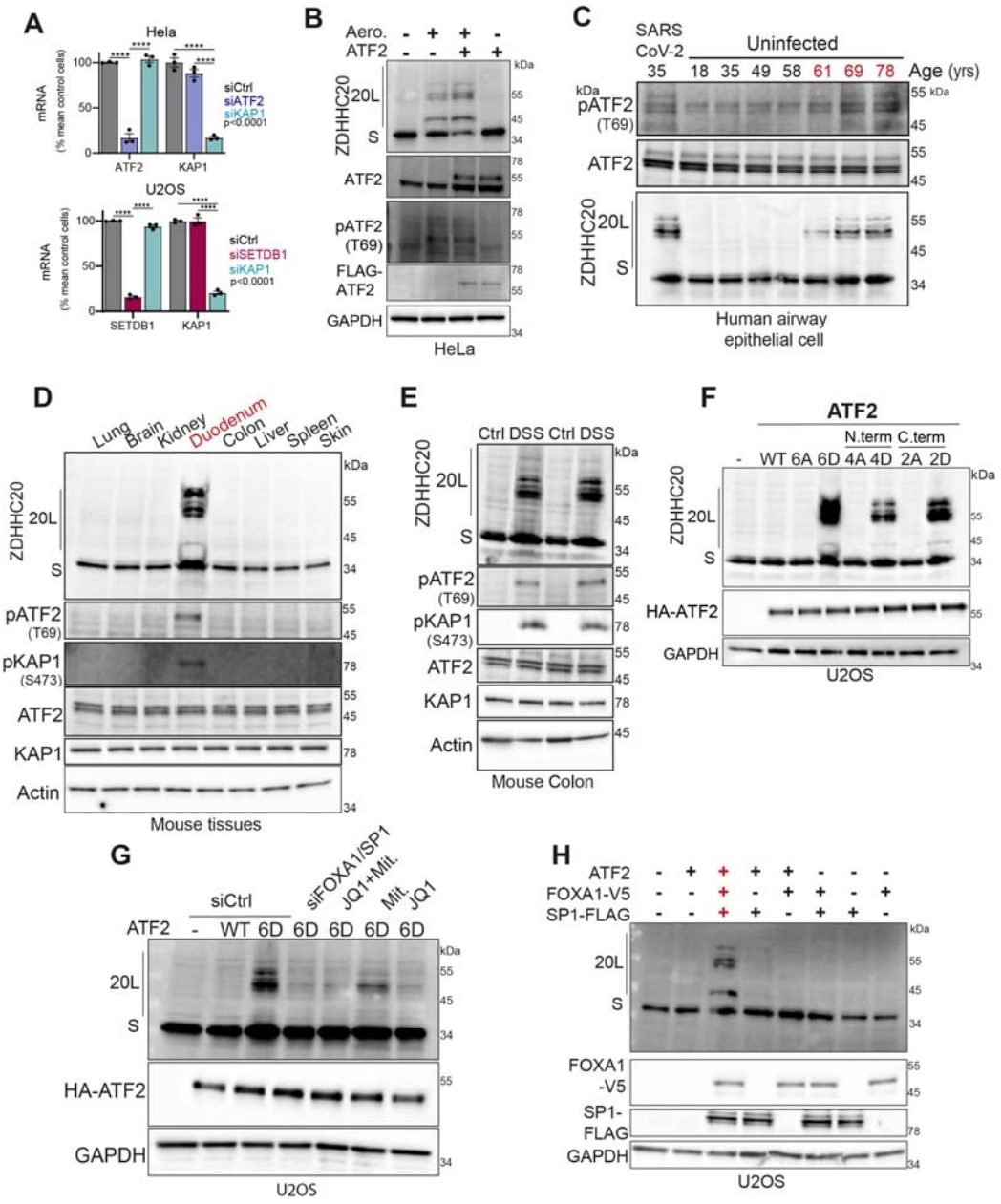

Figure S1. ATF2 and SETDB1-KAP1 dependent induction of ZDHHC20L expression. **A**. mRNA quantification measuring the efficiency of the ATF2, KAP1 and SETDB1 siRNA depletion in U2OS and HeLa cells. **B-F.** WB of ZDHHC20, Short-S and 20L isoforms, total and phospho-ATF2 in lysates from: **B.** HeLa cells over-expressing or not ATF2-HA (24 h), left untreated or treated with 10□ng/ml of proaerolysin (toxin) at 37□°C, washed, and incubated at 37□°C for 8 **C.** primary human airway epithelia extracts depicted in Fig 1B. **D.** Different mouse tissue extracts. **E.** Colon extracts from mice treated or not with DSS for 7 days followed by 3 days recovery. **D-E** with total and phosphor-KAP1. **F.** U2OS cells control (-) or overexpressing the indicated versions of ATF2 (WT, or phosphor mutants 6A, 6D, 4A, 4D, 2A, 2D). **G.** U2OS cells as **F** treated (24□h) with 100□nM JQ1 (FOXA1 inhibitor) or 100□nM mithramycin (SP1 inhibitor) or siRNA depleted for FOX1 and SP1 (72h). **H**. U2OS cells over-expressing (24 h) ATF2-HA, SP1-FLAG and FOXA1-V5, alone or in different combinations.

ZNF354A docks the repressive complex onto the regulatory region of *ZDHHC20L*

KAP1/SETDB1 complexes are generally tethered to DNA by KRAB-containing zinc finger proteins (KZFPs), some 380 of which are encoded by the human genome[55,56,58] (Fig. 1G). To identify the KZFP responsible for docking KAP1 at the *ZDHHC20* locus, we mined KRABopedia, a published ChIP-seq dataset generated from HEK293T cells overexpressing HA-tagged forms of each KZFP individually[59,60]. The binding sites of several KZFPs map to the promoter region of *ZDHHC20* (Fig. 2A, S2A), not an uncommon occurrence with these proteins[59,60]. In contrast, ZNF317, ZNF354A, ZNF677 and ZNF793 have binding sites within the "repression" region of the acyltransferase gene. ZNF354A binding sites co-localize with the SETDB1 and H3K9me3 peaks upstream and downstream of the *ZDHHC20* TSSs (Fig. 2A, S2A). We silenced each of the four KZFPs individually in U2OS cells using mixes of siRNAs (Fig. S2B). Only the ZNF354A knockdown led to the expression of ZDHHC20L (Fig. 2B), which could be reverted by the expression of ZNF354A-HA (Fig. S2C). The specificity for ZNF354A was further established by immunoprecipitation (IP) experiments against KAP1 using U2OS cells overexpressing irrelevant KZFPs. All three KZFPs co-precipitated with KAP1, as the presence of canonical KRAB domains would predict[61]. Interestingly, the interaction between KAP1 and ZNF354A was disrupted by aerolysin treatment, which was not the case for the two other KZPs (Fig. 2C). Therefore, ZNF354A specifically binds DNA to repress ZDHHC20L expression with KAP1 in resting cells, and this complex breaks down upon aerolysin treatment.

Dynamics of a non-canonical KAP1-repressive complex

Since ATF2, KAP1 and ZNF354A bind to the same region within the *ZDHHC20* 5'UTR, we examined if they are part of a single complex. We immunoprecipitated KAP1, in control or aerolysin-treated HeLa cells, that were depleted of endogenous ATF2 using siRNA while overexpressing wild-type or ATF2 phosphorylation mutants (6A, and 6D) together with ZNF354A-FLAG. KAP1 co-precipitated both ZNF354A and ATF2 (Fig. 2D). ATF2 interacted with KAP1 in all conditions tested (Fig. 2D). In contrast, while ZNF354A

associated with KAP1 independently of ATF2, aerolysin and the 6D ATF2 mutant disrupted this interaction (Fig. 2D). ATF2 has not previously been reported to be part of any KAP1-KZFP repressive complex. Therefore, KAP1-ZNF354A and ATF2 form a non-canonical repressive complex, which is sensitive to ATF2 phosphorylation induced upon stress stimuli.

Since ATF2 undergoes phosphorylation upon stress, we wondered whether the same occurs for KAP1 and ZNF354A. KAP1 is known to undergo phosphorylation on Ser-824 and Ser-473 in response to DNA damage[62–65,66] and on Ser-473 under oxidative stress[67]. Using an anti-phospho-Ser-473-KAP1 antibody, we detected KAP1 Ser-473 phosphorylation during SARS-CoV-2 infection, concomitant to ATF2 activation (Fig. 2E). KAP1 Ser-473 phosphorylation was also observed upon aerolysin treatment (Fig. S2D), detected in the duodenum of mice (Fig. S1D), and in the colon of mice upon chemical-induced colitis (Fig. S1.E). To determine whether Ser-473 is the major phosphorylation site we expressed WT KAP1 or the S473A phospho-deficient mutant in cells silenced for the endogenous protein, and exposed them to aerolysin. Western blot analysis of KAP1 IP fractions, using anti-phospho-Ser/Thr antibodies, showed no signal for the S473A mutant (Fig. 2F), validating Ser-473 as the primary phosphorylation site, in our conditions. Finally, we verified that Ser-473 phosphorylation was necessary to trigger ZDHHC20L expression upon aerolysin treatment (Fig. S2E), and as with ATF2, expression of a phospho-mimetic S473D KAP1 mutant was sufficient to enable ZDHHC20L expression and ATF2 phosphorylation without any stimulus (Fig. 2G).

We next probed for the potential phosphorylation of ZNF354A. Aerolysin treatment and SARS-CoV-2 infection both induced serine/threonine phosphorylation of ZNF354A, detected by phospho-Ser/Thr antibodies in ZNF354A-IPs (Fig. 2H). This phosphorylated band was specific to ZNF354A, as it was absent in ZNF354A-silenced cells (Fig. 2H). Aerolysin-induced phosphorylation was not detected for a control KZFP, ZNF793, which failed to co-IP ATF2, and did not dissociate from KAP1 in response to aerolysin (Fig. S2F). Finally, similar to ZDHHC20L expression (Fig. 1E) and the dissociation of the ZNF354A-KAP1 complex (Fig. 2D), aerolysin-induced phosphorylation of KAP1 and ZNF354A depended on ATF2

phosphorylation, which alone was sufficient to drive all these events (Fig. 2J) and also promote SETDB1 dissociation (Fig. S2G).

Together these findings demonstrate that ZDHHC20L expression is repressed by a non-canonical complex containing ATF2, SETDB1, KAP1, and ZNF354A. Upon stress, ATF2, KAP1, and ZNF354A each undergo phosphorylation. ATF2 and KAP1 phosphorylation are required and sufficient to dissociate ZNF354A and activate ZDHHC20L expression (Fig 2J).

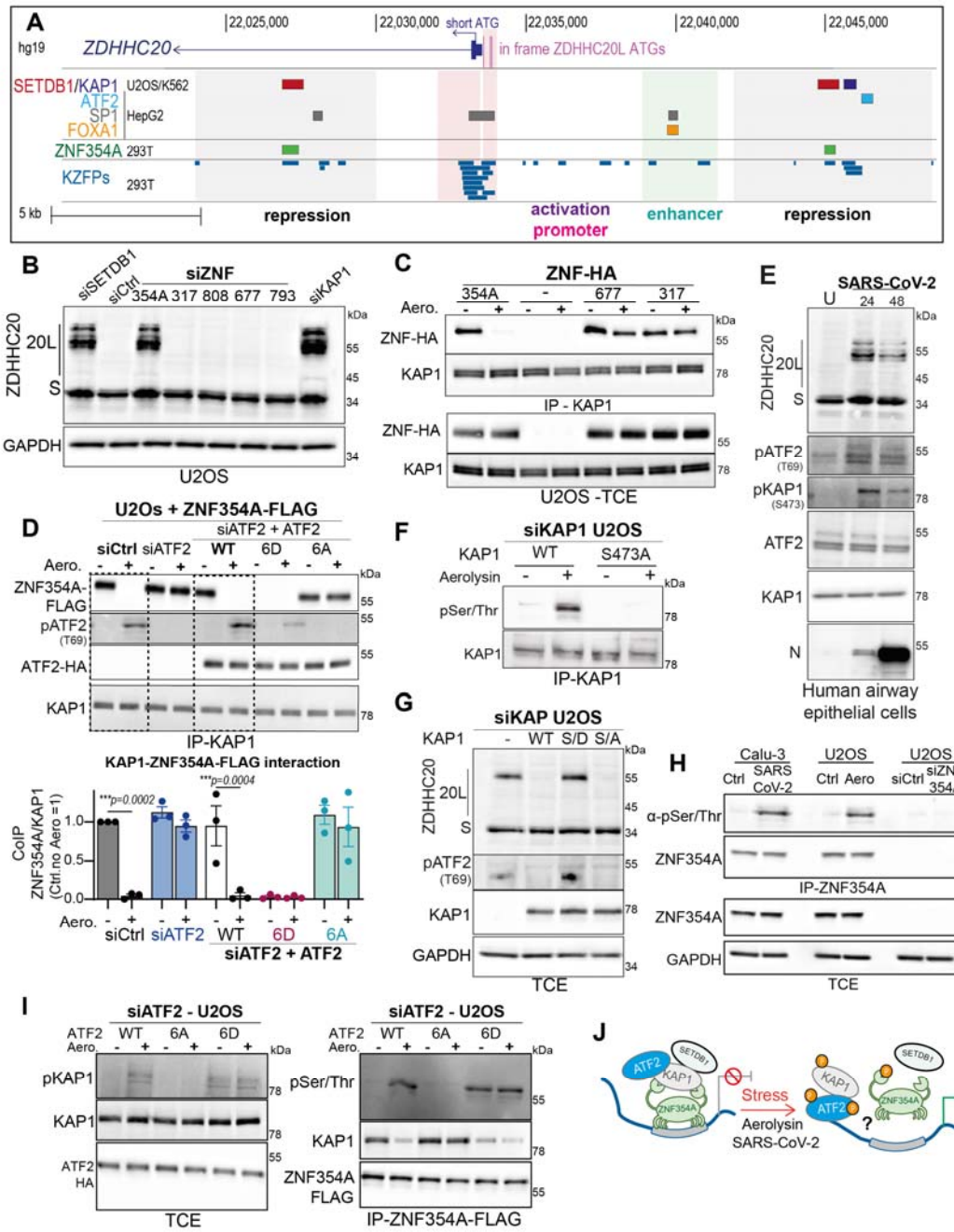
A
hg19
ZDHHC20
short ATG
in frame ZDHHC20L ATGs
22,025,000
22,030,000
22,035,000
22,040,000
22,045,000
SETDB1/KAP1 U2OS/K562
ATF2
SP1 HepG2
FOXA1
ZNF354A 293T
KZFPs 293T
5 kb
repression
activation promoter
enhancer
repression
B
siSETDB1
siCtrl
siZNF
354A 317 808 677 793
siKAP1
ZDHHC20
20L
S
GAPDH
U2OS
C
ZNF-HA
354A
677
317
Aero.
ZNF-HA
KAP1
IP - KAP1
U2OS -TCE
E
SARS-CoV-2
U 24 48
ZDHHC20
20L
S
pATF2 (T69)
pKAP1 (S473)
ATF2
KAP1
N
Human airway epithelial cells
D
U2Os + ZNF354A-FLAG
siATF2 + ATF2
siCtrl siATF2 WT 6D 6A
Aero.
ZNF354A-FLAG
pATF2 (T69)
ATF2-HA
KAP1
IP-KAP1
KAP1-ZNF354A-FLAG interaction
CoIP ZNF354A/KAP1 (Ctrl.no Aero =1)
***p=0.0002
***p=0.0004
siCtrl siATF2 WT 6D 6A
siATF2 + ATF2
F
siKAP1 U2OS
KAP1 WT S473A
Aerolysin
pSer/Thr
KAP1
IP-KAP1
G
siKAP U2OS
KAP1 - WT S/D S/A
ZDHHC20
20L
S
pATF2 (T69)
KAP1
GAPDH
TCE
H
Calu-3
U2OS
U2OS
Ctrl SARS CoV-2
Ctrl Aero
siCtrl siZNF 354A
α-pSer/Thr
ZNF354A
IP-ZNF354A
GAPDH
TCE
I
siATF2 - U2OS
ATF2 WT 6A 6D
Aero.
pKAP1
KAP1
ATF2 HA
TCE
siATF2 - U2OS
pSer/Thr
KAP1
ZNF354A FLAG
IP-ZNF354A-FLAG
J
ATF2
SETDB1
KAP1
ZNF354A
Stress
Aerolysin
SARS-CoV-2
?

Figure 2. ZNF354A controls the expression of stress-induced ZDHHC20L.
A. Overview of the *ZDHHC20* locus (first intron, exon, and 5'UTR - version hg19), Tracks indicate: in-frame transcription start codons (ATGs); transcript (GENCODE-V4 0lift37); SETDB1/KAP1,ATF2, SP1 and FOXA1 ChIP-seq (ENCODE) peaks; ZNF354A and other KZFP ChIP-seq peaks (squish view) from HEK293T cells obtained from KRABopedia (https://tronoapps.epfl.ch/web/krabopedia/) [59] (see also Fig S2A). **B.** WB of ZDHHC20, Short-S and 20L isoforms and GAPDH loading control in U2OS cells depleted for SETDB1, KAP1, and the indicated KZFPs. **C.** Immunoprecipitation (IP) of endogenous KAP1 from U2OS cells over-expressing the indicated HA-tagged KZFPs (ZNF-HA) left untreated or treated 1 h with 10□ng/ml of proaerolysin (toxin) at 37□°C, washed, and incubated at 37□°C for 8 h. Blots show IP-fractions with Co-IP KZFPs and total cell extracts (TCE). **D.** As (C) in siCtrl or siATF2 (72 h) cells overexpressing ZNF354A-FLAG complemented with the indicated ATF2 constructs (WT, 6D or 6A mutants – 24 h). Results are mean□±□SEM; each dot represents one independent experiment (n□=□3); *P* values comparing to untreated (-) obtained by two-way ANOVA, Tukey's correction. **E.** As (B) in human epithelial lung cells infected with SARS-CoV-2 (MOI 0.1). **F.** IP-KAP1, (as D), in U2OS cells siKAP1 (72 h) overexpressing WT or S473A KAP1 mutant treated with aerolysin (as C). Blots show KAP1 and correspondent anti-Ser- and Thr- phosphorylated protein bands (α-pSer/Thr) present in IP-KAP1 fractions **G.** As (B) in siKAP (72) U2OS cells expressing KAP1 WT, S473A-S/A, or S473D-S/D **H**. IP of ZNF354A from Calu-3 cells infected with SARS-CoV-2 (24 h), U2OS cells aerolysin-treated (as C). or U2OS siCtrl or siZNF354A depleted (as C). Blots show ZNF354A and α-pSer/Thr bands in IP-ZNF35A fractions and ZNF354A in TCE. **I.** IP-ZNF-HA in cells expressing the indicated ZNF-FLAG constructs and the indicated ATF2 constructs treated with aerolysin (as C). Blots show KAP1, ATF2, and α-pSer/Thr for IP-ZNF-HA fractions, and phosphor-KAP1 and total KAP1 and ATF2-HA for TCE. **K.** Schematic representation of the ATF2-KAP1-ZNF354A transcription regulation before and after stress conditions.

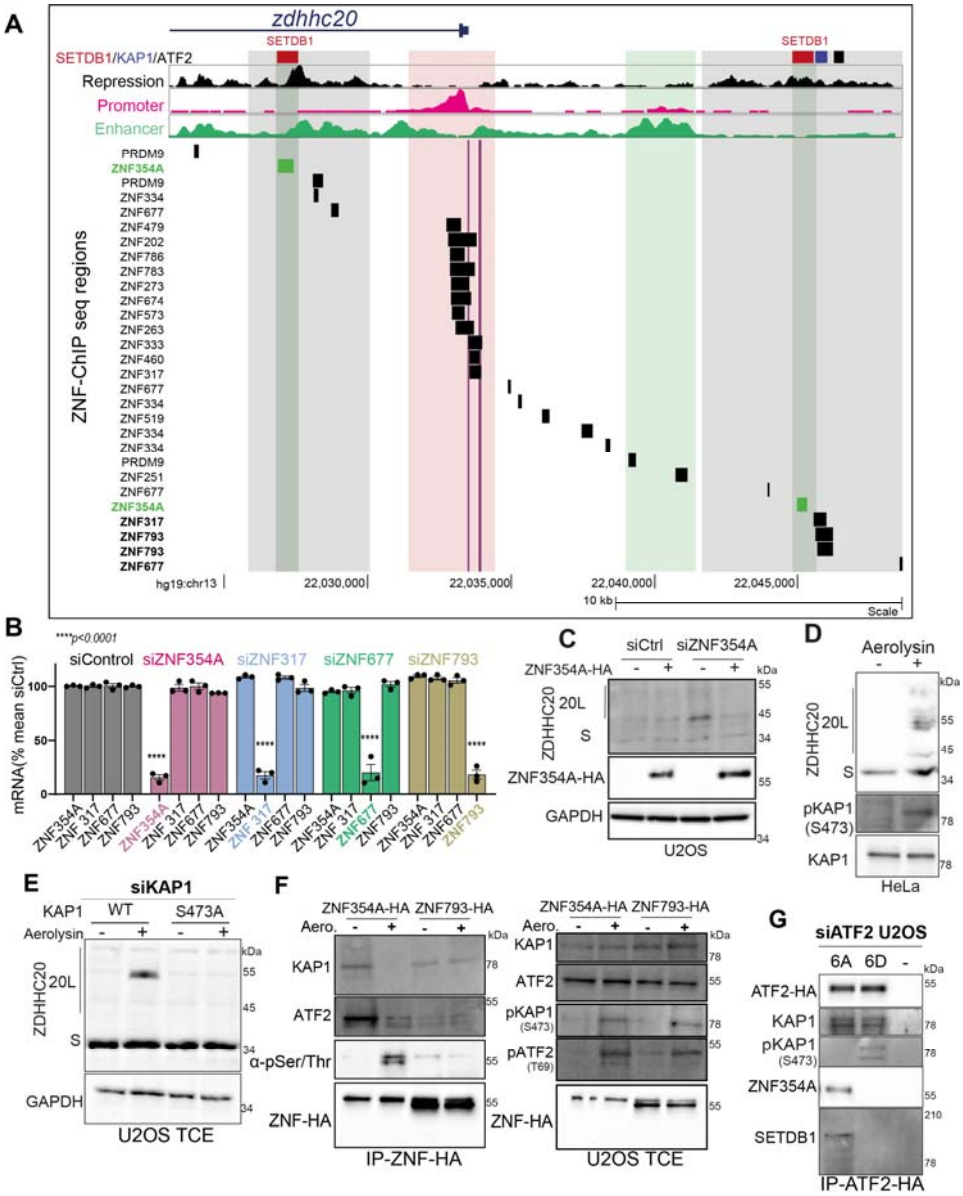

Figure S2. ZNF354A controls expression of stress-induced ZDHHC20L.

A. Overview of the *ZDHHC20* locus (first intron, exon, and 5'UTR - version hg19), Tracks indicate: in-frame transcription start sites (ATGs); transcript (GENCODE-V4 0lift37), various histone modifications ChIP-seq signals (ENCODE/Broad); SETDB1/KAP1/ATF2 ChIP-seq (ENCODE) peaks; ZNF354A and individual KZFP ChIP-seq peaks from HEK293T cells obtained from KRABopedia (https://tronoapps.epfl.ch/web/krabopedia/) [59]. **B.** mRNA quantification probing for the indicated KZFP proteins in U2OS cells siRNA depleted for different KZFP proteins. Results are mean ±□SEM; each dot represents one independent experiment, n=3; *P* values comparing to each siCtrl, were obtained by two-way ANOVA Dunnet's correction. For all other KZFPs data is n=2. **C**. WB of ZDHHC20, Short-S and 20L isoforms, and GAPDH loading control in U2OS cells depleted for ZNF354A complemented with ZNF354A-HA (24 h) **D**. WB as (C) also showing total and phospho-KAP1 levels in HeLa cells untreated or treated with 10□ng/ml of proaerolysin (toxin) at 37□°C, washed, and further incubated at 37□°C for the 8 h. **E.** As (C) in U2OS cells siKAP1 (72 h) overexpressing WT or S473A KAP1 mutant. **F.** IP-ZNF-HA in U2OS cells expressing the indicated ZNF-HA constructs aerolysin-treated as (D). Blots show KAP1, ATF2, and α-pSer/Thr proteins for IP-ZNF-HA fractions, and phospho-ATF2, phospho-KAP1 and total ZNF-HA for TCE. **G.** IP-ATF2-HA in siATF2 U2OS cells (72 h) overexpressing 6A or 6D mutant ATF2-HA. Blots show KAP1, ZNF354A, SETDB1 and pKAP (S473) levels in IP-ATF2-HA fractions.

p38- and JNK-dependent phosphorylation of the repressive complex components

To explore the regulatory mechanisms of the ATF2-KAP1-ZNF354A complex, we first identified the ZNF354A phosphorylation sites. Three residues, located in the linker region between the KAP1-binding KRAB domain and the DNA-binding domains, were found in phospho-proteomics studies in breast cancer (Ser-169 and Thr-185)[68], and a subgroup of large T-cell lymphoma (T154)[69] (https://www.phosphosite.org). We generated the corresponding phospho-mutants and expressed them in ZNF354A-silenced U2OS cells. A clear phosphor-Ser/Thr signal was observed upon aerolysin treatment of WT ZNF354A-, but not S169A ZNF354A-expressing cells (Fig. 3A). The signal was reduced, but not absent, when expressing the T154A or T185A mutants (Fig. 3A), indicating a leading phosphorylation event at Ser169, as confirmed using phospho-tag gels (Fig. 3B).

We next searched for the kinases involved in ZDHHC20L expression. We tested a panel of inhibitors targeting MAPKs (*e.g.* JNK, p38, and ERK) and ATM since these are known to modify KAP1 and ATF2 following different stresses, including infection[70,71]. Inhibition of either p38 or JNK abolished the aerolysin-induced expression of ZDHHC20L and KAP1 phosphorylation, and reduced phosphorylation of ATF2. ATF2 phosphorylation was also sensitive to ERK inhibition (Fig. 3C). p38 and JNK inhibitors similarly affected KAP1 and ZNF354A phosphorylation and ZDHHC20L expression in cells expressing the ATF2 6D mutant, in the absence of stressor (Fig. 3DE). Thus, phosphorylation of ATF2, KAP1 (on Ser-473) and ZNF354 (on Ser-169) occurs in p38- and JNK-dependent manner and is required for the expression of ZDHHC20L.

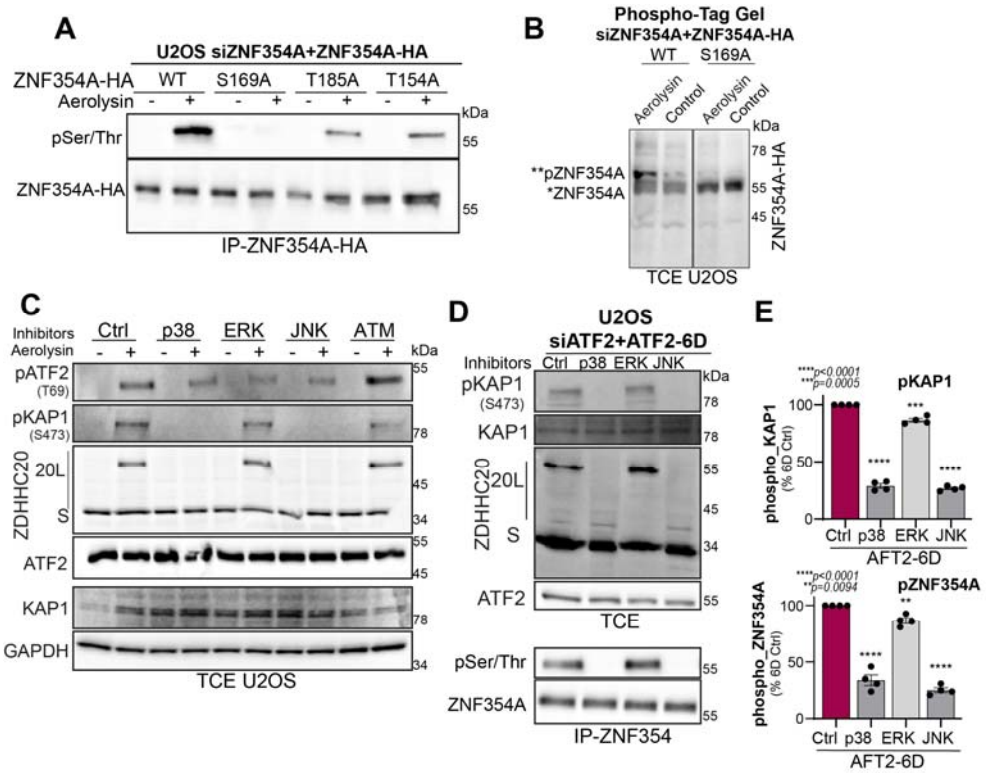

Figure 3. p38 and JNK phosphorylation of ZNF354A

A. IP-ZHF354A-HA, in U2OS cells siZNF354A (72 h) overexpressing WT or the indicated phospho mutants of ZNF354A, left untreated or treated with 10□ng/ml of proaerolysin (toxin) at 37□°C, washed, and further incubated at 37□°C for 8 h. Blots show α-pSer/Thr proteins and ZNF354A in IP-ZNF-HA fractions **B.** Phospho-Tag Western blot (WB) of total cell extracts (TCE) of U2OS treated as (A). **C.** WB of ZDHHC20, Short-S and 20L isoforms, phospho-KAP1 (S473) and -ATF2 (T69), total KAP1 and ATF2 and GAPDH loading control in TCE of U2OS treated with aerolysin as (A) in the presence of the indicated kinase inhibitors. **D.** WB as (C). in TCE or IP-ZNF354A from U2OS cells siATF2 (72 h) overexpressing ATF2-6D phosphomimetic mutant (24 h) in the presence of kinase inhibitors. **E.** phospho-KAP1 and pSer/Thr-ZNF354A band quantification of the blots in (D). Results are mean□±□SEM; each dot represents one independent experiment of n□=□3; *P* values comparing to Control (untreated-Ctrl) were obtained by two-way ANOVA, Dunnet's correction.

ZNF354A is a master regulator of the cellular response to oxidative stress

We next explored whether the de-repression of the ZNF354A-containing supercomplex is coupled with the activation of specific host stress response pathways. To identify genes controlled by ZNF354A, we made use of our ChIP-seq data from HEK293T cells overexpressing HA-tagged ZNF354A, which led to the identification of 1,665 binding sites (KRABopedia - https://tronoapps.epfl.ch/web/krabopedia/). Taking 300 kb from the TSS as a cut-off (or the nearest TSS), we identified 2,116 genes potentially regulated by ZNF354A. By combining GREAT (Genomic Regions Enrichment Annotations) and manual curation, we recognized several enriched pathways, with selenium metabolism standing out due to its connection to defense against ROS (Fig. 4A, S3A). ZNF354A has a mouse orthologue, ZFP354A, to which we extended our analysis by conversion of the human genome coordinates of ZNF354A binding sites to the mouse genome and retrieving approximately 300 binding sites. Our analysis confirmed that the mouse ZFP354A also binds in the vicinity of antioxidant genes (Fig. S3A). Consistently, silencing ZFP354A in mouse cells led to ZDHHC20L expression (Fig. S3B).

Among the genes we found associated with ZNF354A binding sites (Fig. S3A), several are involved in cellular redox homeostasis. These include: *MAT1A* (methionine adenosyltransferase 1A), which synthesizes S-adenosylmethionine, a precursor for GSH biosynthesis[72]; *SLC7A11*, encoding the main subunit of the cystine/glutamate antiporter system x_c^-, essential for GSH production[73]; and *TXNRD1* (thioredoxin reductase-1 and its homolog *TXNRD3*), which can reduce cystine after its uptake by the x_c^- system thereby contributing to GSH synthesis[74]. Amongst the genes, we also found 8 selenoprotein-encoding genes (Fig. S3A). These proteins, of which the human proteome counts 25, contain a selenocysteine in their primary sequence which they use to reduce H□O□ and organic hydroperoxides [12,75].

To test that ZNF354A is indeed a regulator of antioxidant defense genes, we performed RNA-seq upon ZNF354A knockdown in U2OS (Fig. S3C), which led to the identification of 1,223 significantly upregulated genes (fold change >2) (Fig. 4B). Using Gene Set Enrichment

Analysis (GSEA), we found that these genes are involved in protective responses against external insults, including bacteria, viruses and chemical stresses, as well as antioxidant activity, lipid perturbations, the NRF2 pathway (Fig. 4 CD, S3D, and supplementary dataset) [15,19]. We confirmed the RNA-Seq data by quantitative PCR (qPCR) for a selected set of genes: *MATA1*, *SLC7A11*, *TXNRD1*, the redox regulator *GLRX* (Glutaredoxin-1), *SEPHS2* (selenophosphate synthetase) and *FSP1* (Fig. S3E), and at the protein level by western blot for MATA1 (Fig. S3C). We also confirmed that NFR2, a well-established regulator of anti-oxidant responses, is involved in ZDHHC20L expression. While silencing ZNF354A leads to ZDHHC20L expression, this was prevented by the additional silencing of NRF2 (Fig. S3FG). Thus, together with SP1 and FOXA1, NRF2 also positively regulates ZDHHC20L expression.

As predicted by the analysis of the ZNF354A DNA binding regions (Fig. 4A), this KZFP is involved in the repression of genes encoding key antioxidant cellular defense effectors (Fig. 4, S3, and supplementary dataset). Many of its target genes are indeed involved in GSH biosynthesis, iron metabolism, the mevalonate pathway and the NADPH-FSP1-CoQ10 oxidoreductase system, which protects cells from lipid radical-induced damage[21,22] (Fig. 4E). These various independent analyses point towards ZNF354A as a master regulator of oxidant cellular defenses, both selenium/thiol-dependent and -independent, and of the sensitivity of cells to ferroptosis[7,12,76].

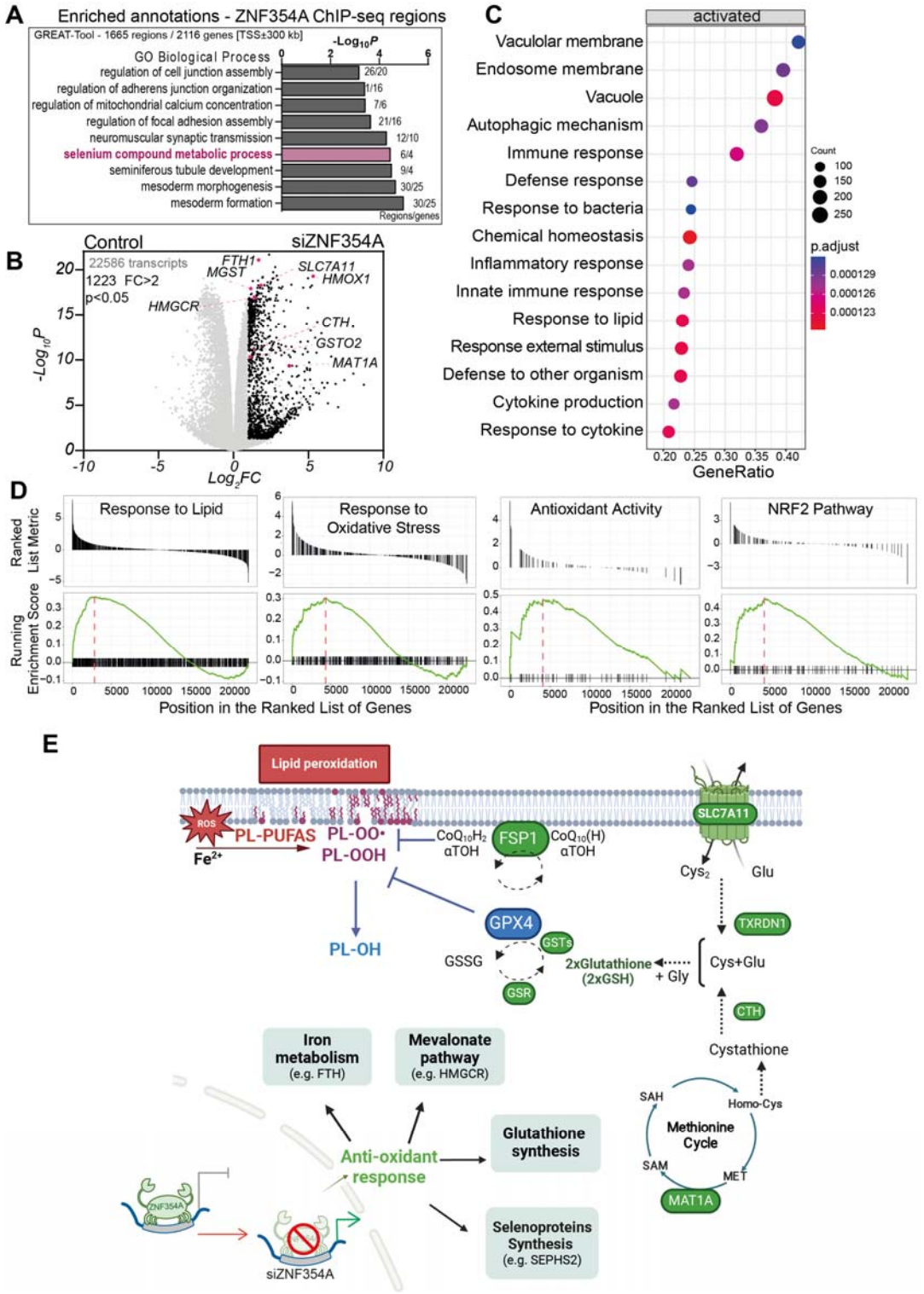
A
Enriched annotations - ZNF354A ChIP-seq regions
GREAT-Tool - 1665 regions / 2116 genes [TSS±300 kb]
GO Biological Process
-Log10P
regulation of cell junction assembly 26/20
regulation of adherens junction organization 1/16
regulation of mitochondrial calcium concentration 7/6
regulation of focal adhesion assembly 21/16
neuromuscular synaptic transmission 12/10
selenium compound metabolic process 6/4
seminiferous tubule development 9/4
mesoderm morphogenesis 30/25
mesoderm formation 30/25
Regions/genes
B
Control
siZNF354A
22586 transcripts
1223 FC>2
p<0.05
FTH1
MGST
SLC7A11
HMOX1
HMGCR
CTH
GSTO2
MAT1A
-Log10P
Log2FC
C
activated
Vaculolar membrane
Endosome membrane
Vacuole
Autophagic mechanism
Immune response
Defense response
Response to bacteria
Chemical homeostasis
Inflammatory response
Innate immune response
Response to lipid
Response external stimulus
Defense to other organism
Cytokine production
Response to cytokine
Count
p.adjust
GeneRatio
D
Response to Lipid
Response to Oxidative Stress
Antioxidant Activity
NRF2 Pathway
Ranked List Metric
Running Enrichment Score
Position in the Ranked List of Genes
E
Lipid peroxidation
ROS
PL-PUFAS
PL-OO•
PL-OOH
Fe2+
CoQ10H2 αTOH
FSP1
CoQ10(H) αTOH
SLC7A11
Cys2
Glu
GPX4
GSTs
GSSG
GSR
PL-OH
2xGlutathione (2xGSH)
+ Gly
Cys+Glu
TXRDN1
CTH
Cystathione
Iron metabolism (e.g. FTH)
Mevalonate pathway (e.g. HMGCR)
Anti-oxidant response
Glutathione synthesis
Selenoproteins Synthesis (e.g. SEPHS2)
SAH
Homo-Cys
Methionine Cycle
SAM
MET
MAT1A
ZNF354A
siZNF354A

Figure 4. ZNF354A is a master regulator of anti-oxidant responses.
A. Ontologies (GREAT analysis) of genomic associations from ZNF354A ChIP-seq in HEK293T cells. Histogram shows enriched terms by *P*-value. **B**. RNA-seq analysis, Volcano plots illustrating the expression of 22586 transcripts between control and siZNF354A (72 h) in U2OS cells. The $\log_2$ fold change (FC) is plotted against the $-\log_{10}$ p value. Black dots represent genes statistically ($P < 0.05$) up-regulated in siZNF354A (FC>2). Selected genes involved in GSH synthesis (*MAT1A, SLC7A11, GSTO2, MGST, CTH*); iron metabolism (*HMOX1, FTH*) and Mevalonate pathway (*HMGCR*) are highlighted. **C**. Gene Set Enrichment Analysis-GSEA dot plot of ZNF354A upregulated enriched GO-terms (abbreviated – full ontologies in Table S2 and supplementary dataset). Gene count, P values and gene ratio (count of enrichment genes) / (count of pathway genes) are indicated. **D.** GSEA plots for the indicated Gene ontologies (GO) for Biological Process (BP), Cell Component (CC). **E**. Overview of ZNF354A-controlled selenium-/thiol-dependent and independent pathways in detoxification of phospholipid peroxides (PL-OOH) with ZNF354A targets depicted in green. Additional proteins involved in ferroptotic-associated defenses including: iron metabolism, selenoprotein synthesis, and the mevalonate pathway, upregulated by siZNF354A are indicated (See also Table S3 and supplementary data set). Thiol-dependent defenses involve GPX4-mediated conversion of PL-OOH (red) to corresponding alcohols (PL-OH). This depends on glutathione (GSH) levels, maintained by cystine uptake through the system xc−, its reduction to cysteine, and subsequent synthesis of GSH by different steps. The methionine cycle contributes with precursors. In parallel the NAD(P)H/FSP1/ubiquinone system reduces peroxyl radicals in phospholipids (PLOO•). SLC7A11, xCT, subunit of system xc-, cystine/glutamate antiporter; TXNRD1, thioredoxin reductase-1, CTH γ-Cystathionase; MAT1A, methionine adenosyltransferase 1A; GSTs, GSH-S-transferases; GSR, GSH-disulfide reductase; GPX4, GSH-peroxidase-4; GSSG, oxidized diglutathione; FSP1, ferroptosis suppressor protein; CoQ10 H2, ubiquinol; CoQ10 (H), ubiquinone/semi-ubiquinone; SEPHS2, selenophosphate synthetase 2; FTH, Ferritin Heavy Chain-1; HMGCR, 3-hydroxy-3-methylglutaryl-CoA reductase. Created with BioRender.com

A

Gene	Gene Name	TSS Distance to ZNF354A peak(s)	Seleno- protein	Redox/Sel function	LiftOver (mouse)
GLRX	Glutaredoxin-1	-24514	no	*S*-(de)glutathionylation	-33670
GPX6	Glutathione peroxidase 6	47542	yes	reduction of hydrogen peroxide.	30098
MAT1A	Methionine Adenosyltransferase 1A	-28062, -16487	no	methionine cycle (synthesis GHS)	n.d.
SELB/EEFSEC	Eukaryotic Elongation Factor, Selenocysteine-TRNA Specific	194202	yes	Sec.tRNA elongation factor	152742
SELS	Selenoprotein S	-12179	yes	reductase	-13661
SEPHS2	Selenophosphate Synthetase 2	15386	yes	synthesis of selenophosphate	13010
SEPP1 (SELP)	Selenoprotein P, Plasma, 1	-121809, -52889	yes	Se transporter protein	n.d.
SEPSECS	Sep (O-Phosphoserine) TRNA:Sec (Selenocysteine) TRNA Synthase	-71731	yes	Selenocysteine synthase	-69778
SLC7A11 (XCT)	Solute Carrier Family 7 (Anionic Amino Acid Transporter Light Chain, Xc- System), Member 11	-114554	no	glutamate-cystine antiporter	n.d.
TXNIP	Thioredoxin-interacting protein (TXNIP)	-1296	no	binds and regulates thioredoxin	-1239
TXNRD1	Thioredoxin Reductase 1	72592	yes	thioredoxinreductase	26264
TXNRD3	Thioredoxin Reductase 3	-35307,65219	yes	thioredoxinreductase	n.d.

Retrieved by GREAT / Manual Curated

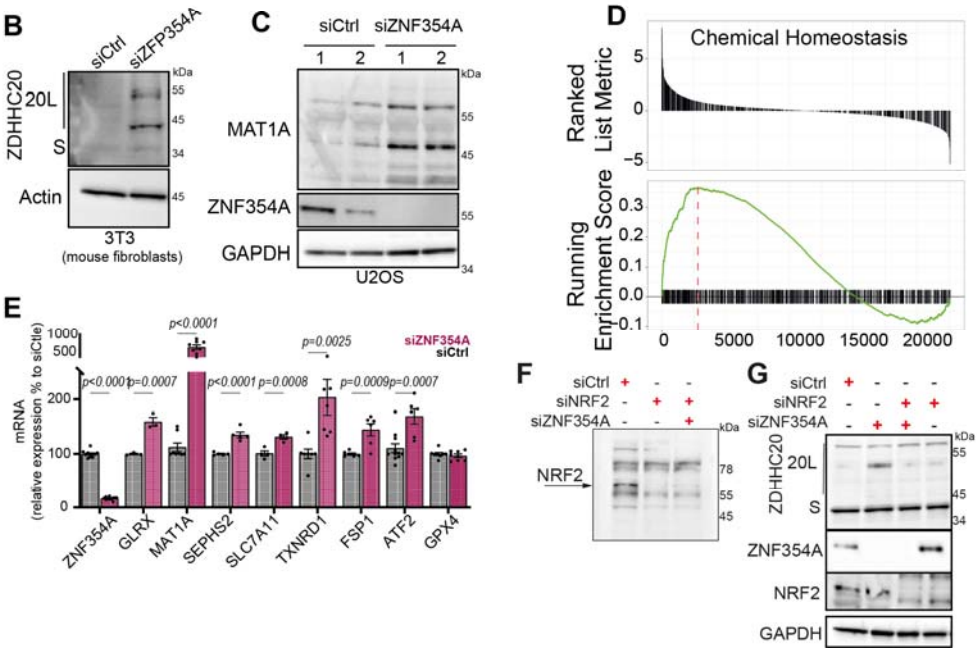

Figure S3. ZNF354A is a master regulator of anti-oxidant responses.
A. Selected examples (GREAT-retrieved-orange or manual curated) of genes associated with Selenium pathways, antioxidant and anti-ferroptotic activity with ZNF354A ChIP-seq within 300 kb from their TSS in HEK293T cells. Gene symbols, gene names, and distance to ZNF354A Chip-seq peaks are indicated. **B C.** Western blot in **B.** 3T3 mouse fibroblasts siCtrl- or siZNF354A- (mouse ZFP354A) -depleted (72 h) or **C**. U2OS cells showing **B**. ZDHHC20 S, and 20L isoforms or **C.** MAT1A and ZNF354A. Actin and GAPDH levels, used as loading controls respectively. **D.** GSEA plots for the indicated Chemical Homeostasis-Gene ontology. mRNA quantification of the indicated transcripts in U2OS cells siCtrl or siZNF354A depleted (72 h). **E.** Results are mean ±□SEM, and each dot represents one independent experiment. *P* obtained by two-way ANOVA Sidak's correction. **F.G.** WB of NRF2, and **G.** ZDHHC20, Short-S and 20L isoforms, ZNF354A and GAPDH loading control in TCE of U2OS siNRF2, siZNF354A or siNRF2/ZNF354A depleted (72 h).

ZDHHC20L expression is induced by lipid peroxidation

Since ZNF354A regulates genes involved in cellular defenses against oxidative damage and ferroptosis, we explored whether oxidative damage could be the common primary trigger of the ZDHHC20L expression observed following SARS-CoV-2 infection, pore-forming toxin treatment, colitis, and aging (Fig. 1). Oxidative damage was induced by treating U2OS cells for 4-8 h with H□O□ at 50 µM, a significantly lower concentration than used to induce DNA damage[14]. ZDHHC20L was expressed in a dose-dependent manner (Fig. 5A).

We next tested whether ZDHHC20L expression could be specifically triggered by inducing the accumulation of membrane lipid peroxides. These form when oxygen radicals interact with PUFA-containing phospholipids[5,13,77]. Under physiological conditions, their accumulation is avoided by the action of GPX4, the primary enzyme that detoxifies lipid peroxides, by reducing them to lipid alcohols[23]. Treating cells with the covalent GPX4 inhibitor RSL3 (RAS-selective-lethal-3) induced ZDHHC20L expression in a dose-dependent manner (Fig. 5B). H□O□ and RSL3 treatment also triggered phosphorylation of ATF2 (Fig. 5B), KAP-1 and ZNF354A (Fig. S4A). Silencing of GPX4 similarly led to ZDHHC20L expression (Fig. 5C). Finally, since GPX4 requires GSH for its reduction, a third way of impairing its activity is to block cystine uptake via SLC7A11 (system Xc^-). Erastin, a system Xc□ inhibitor [78], also induced ZDHHC20L expression in a dose-dependent manner (Fig. S4B).

Upon induction of lipid peroxidation, detoxification can also be performed chemically using lipophilic peroxyl radical-trapping molecules such as Ferrostatin-1 (Fer-1)[79]. Ferrostatin 1 inhibited the H□O□ -induced expression of ZDHHC20L in dose-dependent manners (Fig. 5D). Importantly, ferrostatin also inhibited aerolysin-induced ATF2 and KAP1 phosphorylation, and ZDHHC20L expression (Fig. 5E). Thus, inducing lipid peroxide accumulation leads to ZDHHC20L expression, and prevents the accumulation using Ferrostatin-1 blocks this process.

We next verified whether H□O□ could fully recapitulate the events triggered by aerolysin exposure or SARS-CoV2 infection. H□O□ treatment led to the phosphorylation of ATF2,

KAP1 (on Ser-473), and ZNF354A (on Ser-169) (Fig. 6A-C), in a ferrostatin-dependent manner (Fig. S4A). H□O□ -induced ZDHHC20L expression was prevented by the expression of both the phospho-deficient KAP1 S473A and ZNF354A S169A mutants (Fig. S5DE). The H□O□ -induced ATF2, KAP1 and ZNF354A phosphorylation and ZDHHC20L expression were p38- and JNK-dependent (Fig. 6AB). Inhibition of ERK also reduced ATF2 and more mildly ZNF354A phosphorylation, without affecting KAP1 phosphorylation or ZDHHC20L expression (Fig. 6AB). ATM inhibition mildly reduced phosphorylation of all three components, and the expression of ZDHHC20L (Fig. 6AB). Finally, H□O□ treatment led to the separation of ZNF354A and SETDB1 from the repressive complex (Fig. 6C).

Altogether these observations demonstrate that H□O□ induces lipid peroxidation, which in turn triggers the expression of ZDHHC20L through the p38/JNK-dependent phosphorylation of ATF2, KAP1 (Ser-473) and ZNF354A (Ser-169).

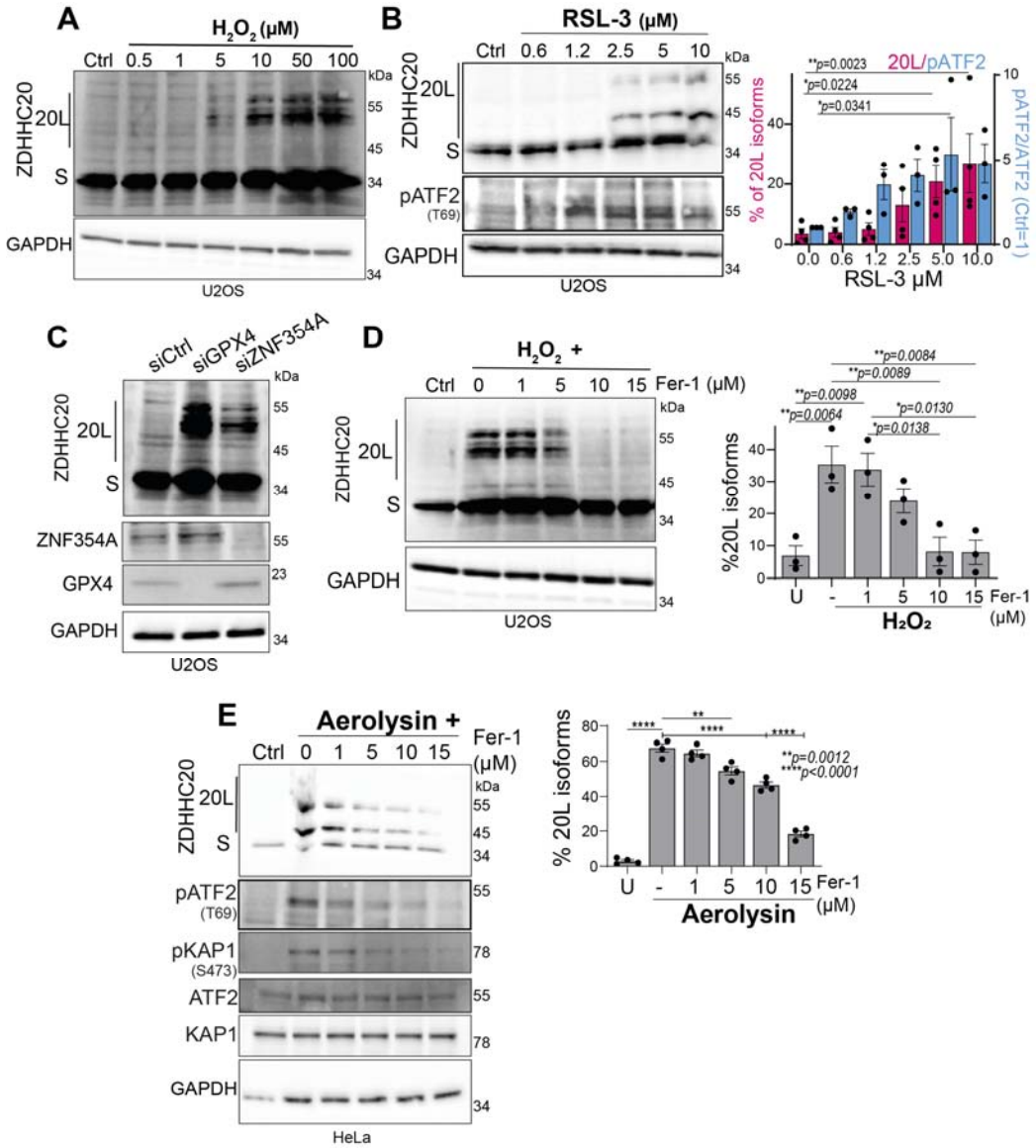

Figure 5. ZDHHC20L and ZNF354A respond to redox homeostasis and lipid peroxidation.

A-E. WB of ZDHHC20 and GAPDH (loading control) in U2OS cells left untreated (Ctrl) or treated with: **A**. increasing concentrations of H□O□ for 8 h, or **B.** increasing concentration of RSL3. **C**. siControl, siGPX4- or siZNF354A (72 h). **D.** 50 μM H□O□ in the presence of increasing concentrations of Ferrostatin-1 (Fer-1); and **E.** HeLa cells treated with 10□ng/ml of proaerolysin (toxin) at 37□°C, washed, and further incubated at 37□°C for the 8 h. For **B**.**D**. and **E.** the % of 20L isoforms, and ATF2 levels corresponds to mean ±□SEM; each dot represents one independent experiment; p values were obtained by two-way ANOVA, Tukey's correction.

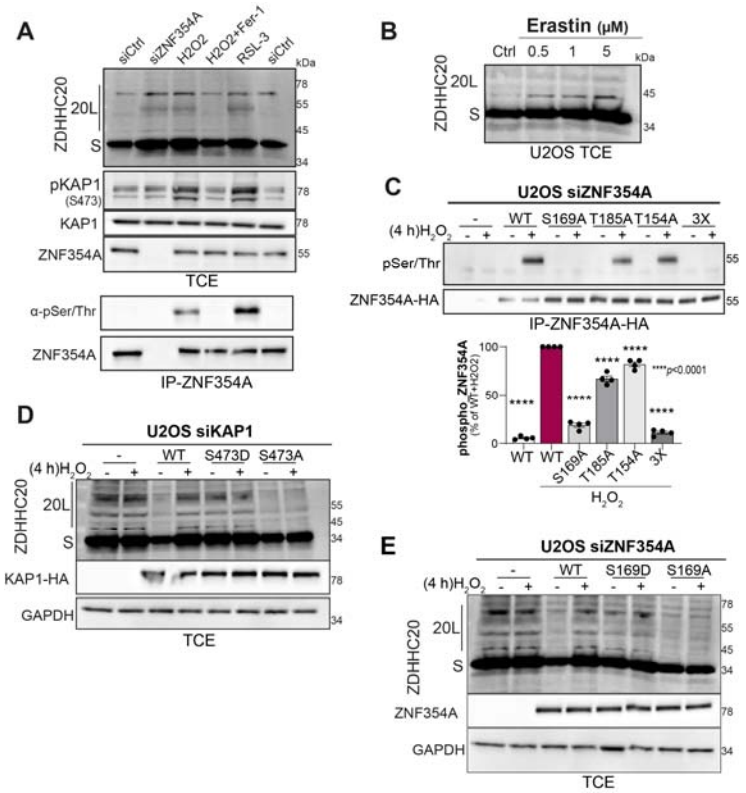

Figure S4. ZDHHC20L and ZNF354A respond to redox homeostasis and lipid peroxidation.

A. Western blot (WB) of**:** total cell extracts (TCE) and Immunoprecipitation (IP)-ZNF354A fractions showing: TCE, ZDHHC20 (20L and S), phospho-KAP1, total-KAP1 and GAPDH (loading control) or IP-ZNF354A, pSer/Thr proteins and ZNF354A, from U2OS cells siCtrl, siZNF254A (72 h), H□O□ (50 μM for 7 h ± Ferrostatin-1,15 μM) and RSL3 (3 μM, 7 h). **B.** WB as (A) showing ZDHHC20 (S and 20L) in TCE from U2OS treated with increasing concentration of Erastin (for 16 h). **C.** IP-ZHF354A-HA, in U2OS cells siZNF354A (72 h) overexpressing WT or the indicated phospho-mutants of ZNF354A (3X-triple mutant with all phospho-residues mutated to Ala, left untreated or treated with H□O□ (50 μM 4 h). pSer/Thr/ZNF354A band quantification. Results are mean□±□SEM; each dot represents one independent experiment of n□=□3; *P* values comparing to WT-expressing H□O□-treated were obtained by two-way ANOVA, Dunnet's correction. **D.** WB as in A in U2OS cells siKAP1 (72 h) expressing the WT KAP1 or the indicated phospho-mutants, left untreated or treated with H□O□ as (C). **E.** WB as(D) in siZNF354A expressing WT of the indicated phospho-mutants of ZNF354A treated as (C).

H□O□ triggers the release of ZNF354A from regulatory loci

Thus far, our data indicate that the repressive complex is composed of ATF2-SETDB1-KAP1-ZNF354A, and that upon lipid peroxidation-induced phosphorylation, the ATF2-SETDB1-KAP1 subcomplex detaches from ZNF354A. We next tested whether under these conditions ZNF354A is released from the DNA to enable expression of the previously repressed genes. We performed genome-wide profiling of ZNF354A binding upon its overexpressed in K562 cells, treated or not with H□O□ for 4 hours (Fig. S5AB). As a preamble, we examined the genomic recruitment of this ZNF354A in untreated cells, and found it to be consistent with that previously recorded in 293T cells, with 20% of K562 peaks (306/1558) already identified in this other cell line (Fig S5C), representing a significant overlap compared to randomized regions (permutation test: 100 permutations, empirical *P*-value = 0) (Fig. S5C). Additionally, the ZNF354A-HA signal intensity over peaks was highly consistent between the ChIP-seq experiments in the two cell lines (Fig. 6D). H□O□ treatment triggered ZDHHC20L expression and ZNF354A phosphorylation (Fig S5B). This correlated with a severe drop in the number of ZNF354A-HA peaks (521 vs. 1558 peaks), and a significantly lower overlap with the peaks previously identified in HEK293T (6% vs. 20%, Fisher's exact test, *P*-value = 2.465e-16) (Fig. 6D). Moreover, ZNF354A occupancy was significantly reduced at the majority of identified peaks (Fig. 6E, S5C). That ZNF354A detaches from the DNA sites upon H□O□ treatment was confirmed by ChIP-RT-qPCR for specific peaks associated with selected redox gene targets *MAT1A*, *SEL1L*, *TXNRD1* and *ZDHHC20* (Fig. 6F). Together, these findings demonstrate that H□O□ treatment leads to the chromatin eviction of ZNF354A, allowing expression of previously repressed genes, notably those involved in antioxidant response.

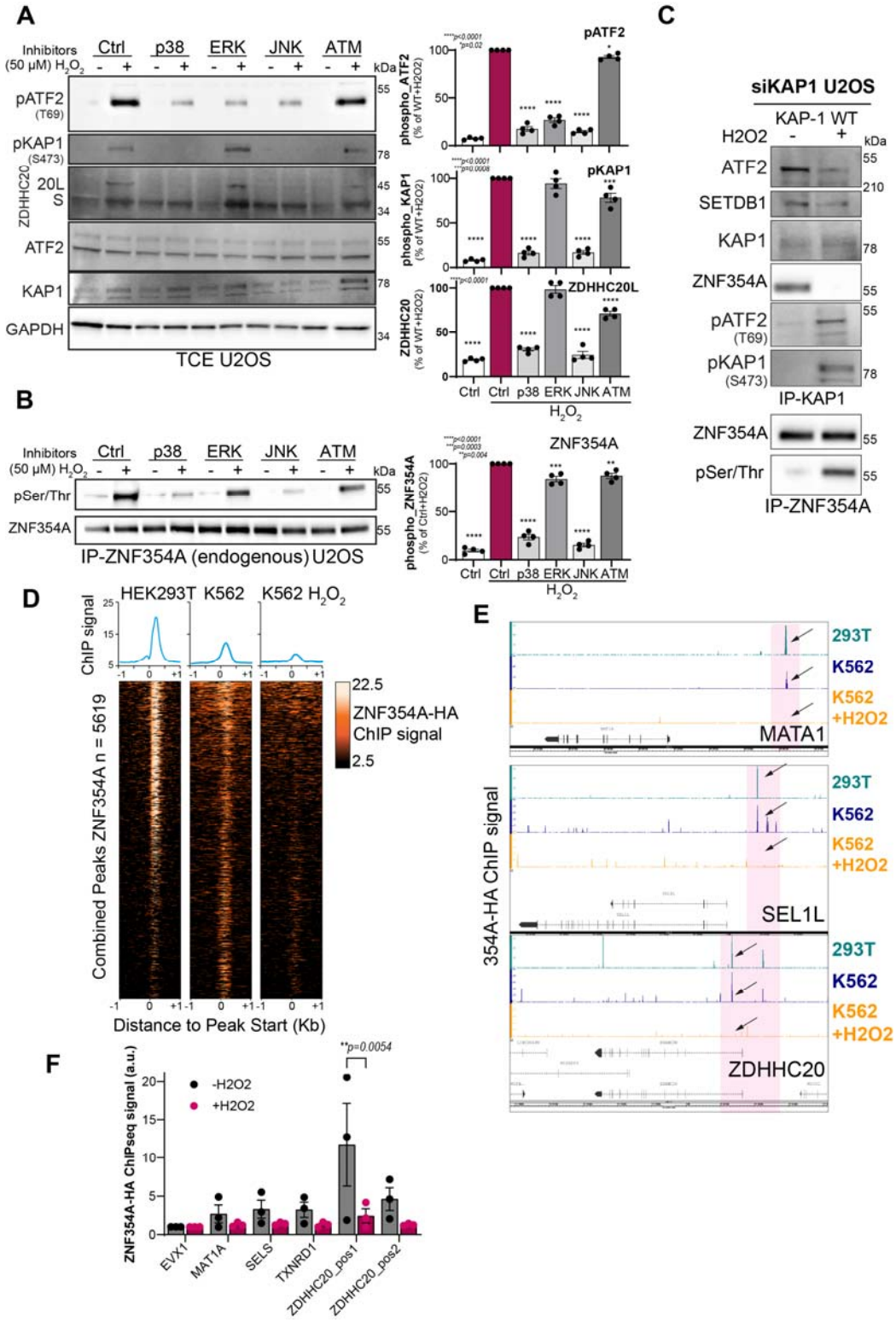
A
Inhibitors
(50 μM) H2O2
Ctrl
p38
ERK
JNK
ATM
kDa
pATF2 (T69)
pKAP1 (S473)
ZDHHC20 20L S
ATF2
KAP1
GAPDH
TCE U2OS
pATF2
pKAP1
ZDHHC20L
phospho_ATF2 (% of WT+H2O2)
phospho_KAP1 (% of WT+H2O2)
ZDHHC20 (% of WT+H2O2)
H2O2
B
pSer/Thr
ZNF354A
IP-ZNF354A (endogenous) U2OS
phospho_ZNF354A (% of Ctrl+H2O2)
C
siKAP1 U2OS
KAP-1 WT
H2O2
ATF2
SETDB1
KAP1
ZNF354A
pATF2 (T69)
pKAP1 (S473)
IP-KAP1
pSer/Thr
IP-ZNF354A
D
HEK293T
K562
K562 H2O2
ChIP signal
ZNF354A-HA ChIP signal
Combined Peaks ZNF354A n = 5619
Distance to Peak Start (Kb)
E
293T
K562
K562 +H2O2
MATA1
SEL1L
ZDHHC20
354A-HA ChIP signal
F
-H2O2
+H2O2
**p=0.0054
ZNF354A-HA ChIPseq signal (a.u.)
EVX1
MAT1A
SELS
TXNRD1
ZDHHC20_pos1
ZDHHC20_pos2

Figure 6. H□O□-dependent regulation of the ATF2-KAP1-ZNF354A epigenetic complex.

A. Western blot (WB) of ZDHHC20, Short-S and 20L isoforms, phospho-KAP1 (S473) and -ATF2 (T69), total KAP1 and ATF2 and GAPDH loading control in TCE or **B.** of pSer/Thr proteins and total ZNF354A from U2OS treated with H□O□ (50 μM, 4 h) in the presence of the indicated kinase inhibitors. **A.** phospho-ATF2, phospho-KAP1, ZDHHC20L and **B.** pSer/Thr/ZNF354A band quantification. Results are mean□±□SEM; each dot represents one independent experiment of n□=□3; *P* values comparing to Control (untreated-Ctrl) were obtained by two-way ANOVA, Dunnet's correction. **C.** WB as (A) also probing for SETB1 of IP-KAP1 or IPZNF354A fractions from siKAP1 cells (72 h) treated with H□O□ as (A). **D.** Profile heat maps centered on ZNF354A-HA ChIP-seq peaks (± 1 kb) with color gradients corresponding to enrichment levels. The dataset includes peaks associated with ZNF354A in HEK293T and K562 cells under untreated and H□O□-treated conditions (50 μM, 4 h). **E.** IGV browser screenshots showing tracks for selected ZNF354 ChIP-seq peaks (arrows) within *MAT1A*, *SEL1L*, and *ZDHHC20* locus from cells treated as in **D. F.** ChIP-qPCR quantification of selected ZNF354A-HA peaks using primers for regions associated with the indicated genes (two peaks were analyzed for ZDHHC20). EVX1 primers were used as controls. Results are mean ± SEM; each dot represents one independent experiment (n = 3). *P* values, compared to untreated (-H□O□), were determined by two-way ANOVA with Tukey's correction.

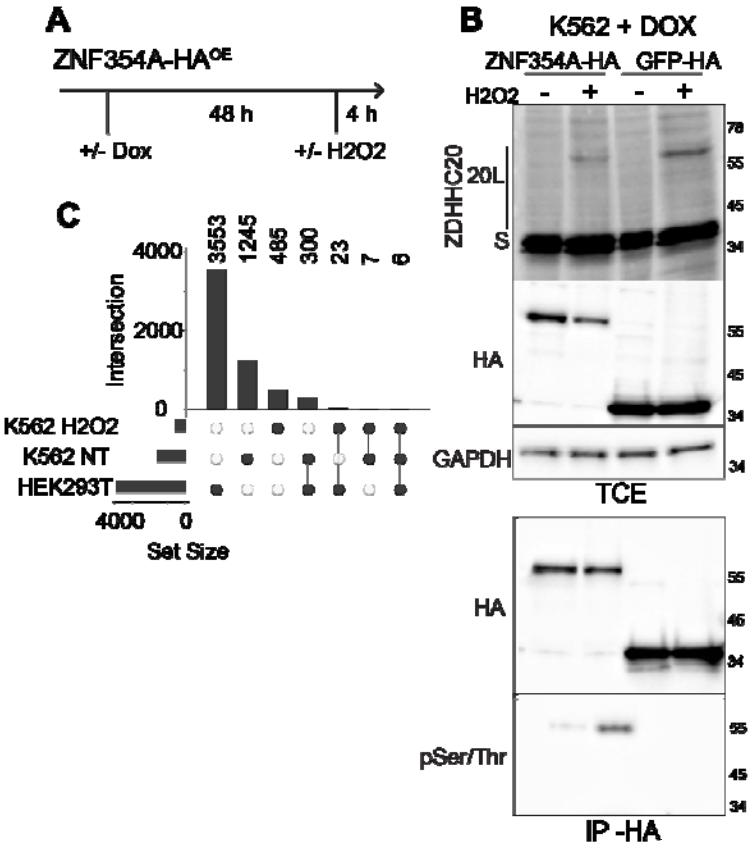

Figure S5. H□O□-dependent regulation of the ATF2-KAP1-ZNF354A epigenetic complex.

A. Schematic of the ChIP-seq experiment using K562 cells stably expressing control GFP-HA or ZNF354A-HA. ZNF354A expression was induced with doxycycline (1 μg/ml) and verified by Western blot (WB). After 48 h, cells were left untreated or treated with H□O□ (50 μM, 4 h). **B.** WB analysis of total cell extracts (TCE) showing ZDHHC20 (short and 20L isoforms), equivalent HA-tagged protein levels, and GAPDH as a loading control. Immunoprecipitated HA (IP-HA) fractions from K562 cells in (A) were analyzed for HA-tagged protein and phospho-Ser/Thr proteins. **C.** UpSet plot illustrating the overlap of ZNF354A binding sites across experimental conditions. The plot depicts the distribution of ZNF354A ChIP-seq peaks identified in HEK293T cells (HEK293T), untreated K562 cells (K562_NT), and H□O□-treated K562 cells (K562_H□O□ - 50 μM, 4 h). Horizontal bars represent the total number of peaks detected in each condition, while vertical bars indicate the number of shared peaks between conditions.

ZNF354A regulates cell sensitivity to ferroptosis

Having identified a ZNF354A-regulated anti-oxidant gene program, we tested whether silencing ZNF354A expression would indeed protect cells from lipid peroxidation-induced death. We first monitored lipid peroxidation itself, using two different fluorescent probes – C11-BODIPY and LiperFluo–, the latter specifically detecting oxidized phospholipids[80,81]. Silencing ZNF354A expression did not affect basal lipid peroxide levels, as detected by both probes (Fig. 7AB). However, ZNF354A-depleted cells showed reduced lipid peroxide accumulation following GPX4 inhibition with RSL3 compared to controls (Fig. 7AB). Consistently, staining with the membrane-impermeant dye propidium iodide (PI) was lower in ZNF354A-depleted cells than in control cells (Fig. 7C). Cell viability was next monitored by measuring ATP levels, following RSL3 or H_2O_2 treatment. Depletion of ZNF354A by siRNA led to a marked increase in viability in response to both RSL3 and H_2O_2 (Fig 7D). Silencing ZNF354A also provided increased cellular resilience to inhibition of cystine import by Erastin (Fig. S6A).

These observations show that silencing ZNF354A expression protects cells from ferroptosis. We tested whether ZNF354A overexpression would sensitize them. To test this, we first designed inactive ZNF354A mutants by mutating the ZFP-KRAB-A box of ZNF354A, a well-conserved interaction domain of KZFP with KAP1 (Fig. S7B) [61], composed in particular of D18, E27, N45 and E46 [61,82,83]. We generated two ZNF354A double mutant constructs with either arginine substitutions of D18 and E27, or arginine and alanine substitutions of N45 and E46, as well as the corresponding quadruple mutant (Fig. S7B). While all constructs were equivalently expressed in HeLa cells, only wild-type ZNF354A efficiently co-immunoprecipitated with KAP1, an interaction that was disrupted by aerolysin treatment (Fig S6A).

We next overexpressed wild-type ZNF354A or the quadruple KAP1-binding deficient mutant ($ZNF354A^{Mut}$) (Fig. S6D). Overexpression of $ZNF354A^{WT}$, but not $ZNF354A^{Mut}$, led to an increase in oxidized phospholipids (Fig. 7E). Consistently, significant cell death could be observed starting at 48 hours of $ZNF354A^{WT}$, but not $ZNF354A^{Mut}$, overexpression (Fig 7F).

Cell viability could be rescued by ferrostatin-1 treatment given twice (at the start of the experiment and after 48 hours) (Fig. 7E), or at a single dose (Fig. S6EF). Thus, ZNF354A^{WT} overexpression leads to lipid peroxide accumulation-induced cell death.

As mentioned earlier, lipid peroxide detoxification relies mostly on GPX4 and FSP1, the latter operating in a GSH-independent manner via the NAD(P)H/FSP1/CoQ10 axis. We tested whether cell death induced by ZNF354A overexpression could be rescued by co-overexpression with either GPX4 or FSP1. FSP1 restored the viability of ZNF354A-overexpressing cells, while GPX4 did not (Fig. 7G). Since the latter might be due to insufficient GSH levels, we supplemented cells with N-acetylcysteine amide (NAC), a cell-permeable cysteine derivative that restores GSH production. NAC in itself was in fact sufficient to rescue ZNF354A-induced cell death, indicating that cellular GPX4 levels were not limiting (Fig. 7G). These findings indicate that ZNF354A overexpression sensitizes cells to lipid peroxidation-induced cell death by impairing lipid detoxification defenses, particularly by reducing the cellular thiol content.

The induction of ferroptosis, a lipid peroxide-induced cell death, is of major interest to kill cancer cells[25] . To investigate the relevance of the LORD pathway in predicting and controlling the sensitivity of tumor cell lines to ferroptosis, we first probed for the phosphorylation of ZNF354A. Only the cells expressing ZDHHC20L, i.e. HEPG2, MCF7 and HCT116 (Fig. 1A, 7H), contained detectable levels of phosphorylated ZNF354A, despite similar ZNF354A expression levels in all cells (Fig. 7H). We next submitted all cell lines to H□O□ or RSL3 treatment, and monitored cell viability by measuring intracellular ATP levels. Consistent with our hypothesis, HEPG2, MCF7 and HCT116 cells were more resistant to either RLS3 or H□O□ , compared to all other lines (Fig. 7I).

Altogether, these observations show that ZNF354 controls the cell's lipid peroxide detoxification capacity, and thereby its sensitivity to ferroptosis. In the context of cancer, the presence of phospho-ZNF354A or ZDHHC20L are therefore predictive of a tumor cell sensitivity to ferroptosis-inducing drugs.

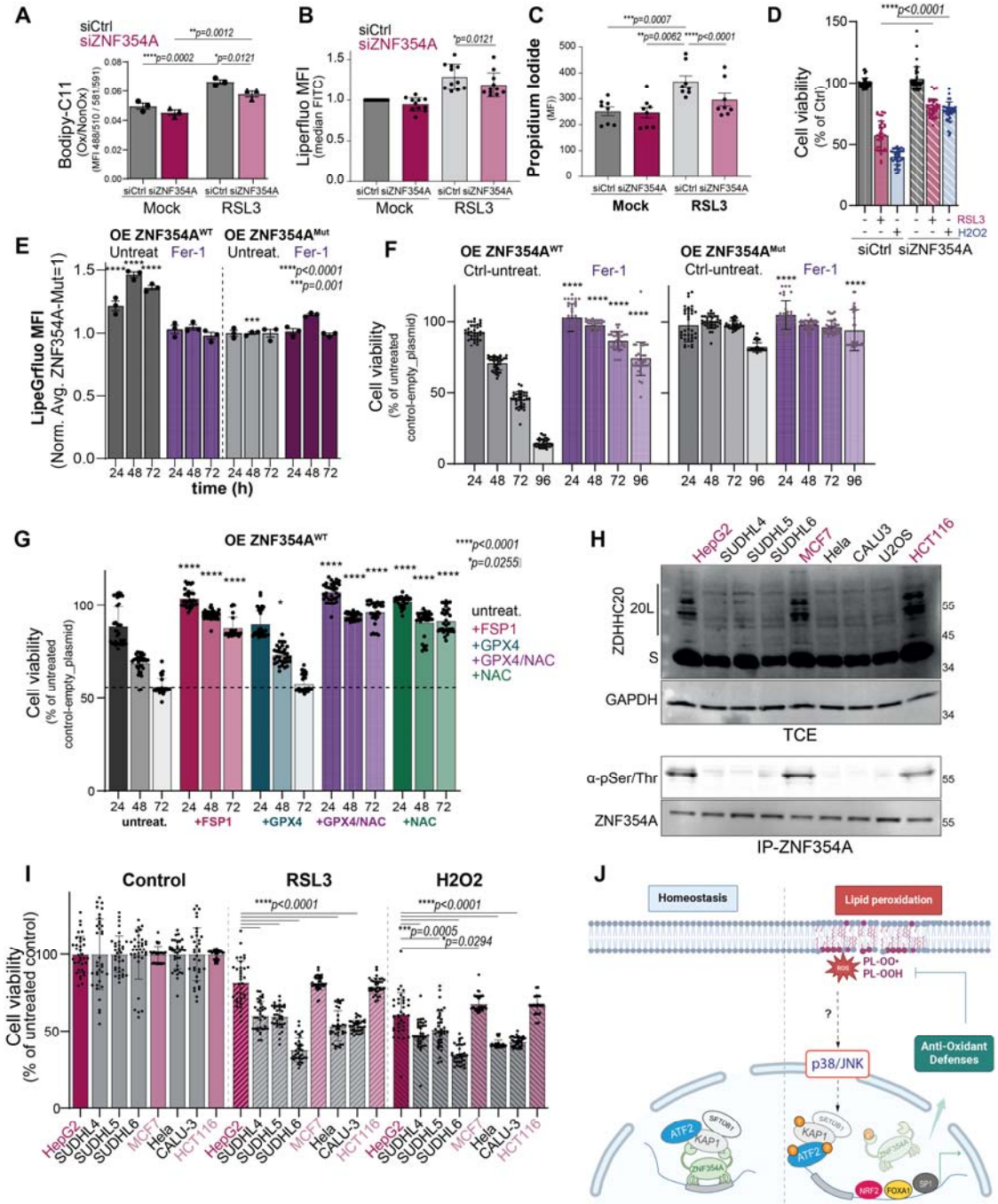
A
siCtrl
siZNF354A
Bodipy-C11 (Ox/NonOx)
Mock
RSL3
B
Liperfluo MFI (median FITC)
C
Propidium Iodide (MFI)
D
Cell viability (% of Ctrl)
RSL3
H2O2
siCtrl siZNF354A
E
OE ZNF354A^WT
OE ZNF354A^Mut
Untreat
Fer-1
LipeGrfluo MFI (Norm. Avg. ZNF354A-Mut=1)
time (h)
F
Ctrl-untreat.
Cell viability (% of untreated control-empty_plasmid)
G
untreat.
+FSP1
+GPX4
+GPX4/NAC
+NAC
H
HepG2
SUDHL4
SUDHL5
SUDHL6
MCF7
Hela
CALU3
U2OS
HCT116
ZDHHC20
20L
S
GAPDH
TCE
α-pSer/Thr
ZNF354A
IP-ZNF354A
I
Control
RSL3
H2O2
Cell viability (% of untreated control)
J
Homeostasis
Lipid peroxidation
PL-OO•
PL-OOH
p38/JNK
Anti-Oxidant Defenses
ATF2
KAP1
ZNF354A
NRF2
FOXA1
SP1

Figure 7. ZNF354A controls lipid peroxide detoxification and sensitivity to ferroptosis. **A-C.** U2OS cells siControl or siZNF354A depleted (72 h) were mock-treated or treated with RSL3 (3 μM) for 24 h. **A.B.** Lipid peroxides were monitored by flow cytometry using Bodipy-C11 or Liperfluo probes. **C.** Membrane permeability was assessed using propidium iodide. Results are mean ± SEM; each dot represents one biologically independent experiment; *P* values were obtained by two-way ANOVA, Tukey's correction**. D.** U2OS cells, siControl or siZNF354A depleted (72 h) were mock-treated or treated with RSL3 (3 μM) or H□O□ (50 μM) for 16 hrs. Cell viability was measured by ATP detection using Promega Glo. Results are mean ±□SD of one representative assay (of three) n=36. *P* values (siCtrl vs siZNF354A) were calculated using two-way ANOVA, Sidak's correction. **E.F.** U2OS cells overexpressing ZNF354A WT or KRAB binding deficient mutant treated ± ferrostatin-1 (15 μM) at time 0 and 48 h post-transfection. **E.** Lipid peroxidation monitored using the Liperfluo probe and flow cytometry. Results are mean ±□SEM and each dot represents a biologically independent experiment; *P* values (Untreated controls vs Fer-1) were obtained by two-way ANOVA, Sidak's correction **F.** Cell viability was monitored as in D. normalized to untreated controls expressing empty plasmid set to 100% (See Fig S6E). Results are mean ±□SD from one, of three, representative assay n=35.*P* values, (Untreated controls vs Fer-1) were obtained by two-way ANOVA, Sidak's correction. **G**. Cell viability monitored as in F in HeLa cells overexpressing ZNF354A, complemented with FSP1, GPX4, GPX4 supplemented with N-Acetyl-Cysteine (NAC, 1 mM), or NAC alone. Results are mean ±□SD from one, of three, representative assay n=33. *P* values (Untreated control for each time point) were obtained by two-way ANOVA, Sidak's correction **H.** Western blot analysis of total cell lysates (TCE) and corresponding ZNF354A-Immunoprecipitation (IP) fractions from a panel of the indicated cancer cell used in Fig 1. Blots show, Short-S (42 KDa) and 20L (~49, 62 and 69 KDa), GAPDH (loading control) for TCE and total ZNF354A and anti-phospho Ser/Thr proteins in ZNF354A IP fraction. **I.** The cancer cell lines in **H** were treated or not with RSL3 (3 μM) or H□O□ (50 μM) for 16 hrs and cell viability was monitored as in **D.** Measurements were normalized to 100 % for each cell type for untreated conditions. Results are mean ±□SD of one representative assay n=35 replicates; p values, comparing to HepG2 (used as reference ZDHHC20L-expressing cell line) for each condition were obtained by two-way ANOVA, Dunnett's correction. **J.** Proposed Model. Under homeostasis, a complex formed by ATF2-SETDB1-KAP1-ZNF354A represses genes involved in antioxidant defenses. Lipid peroxide accumulation triggers an unknown signal that leads to p38/JNK-dependent phosphorylation of ATF2 at the activating T69 residue and subsequent phosphorylation of KAP1 (S473) and ZNF354A (S169). This leads to the dissociation of the SETDB1 and ZNF354A from the complex and DNA targets. This cascade de-represses ZNF354A-regulated genes, activating host defenses against oxidative stress, lipid peroxides, and chemical or pathogenic insults.

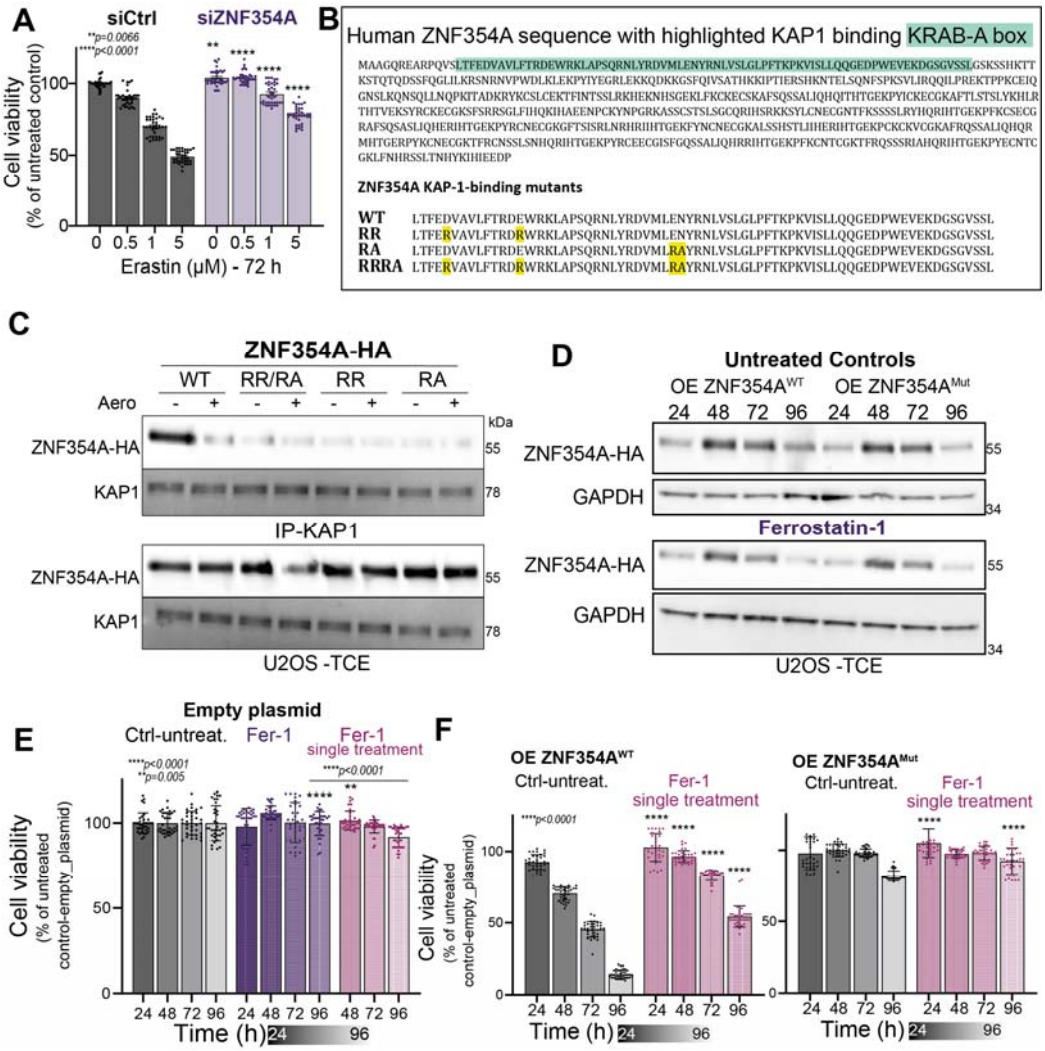

Figure S6. ZNF354A controls lipid peroxide detoxification and sensitivity to ferroptosis. **B.** ZNF354A protein sequence with highlighted (green) KAP1 binding KRAB-A box, and generated KAP1-binding mutants. **C.** Immunoprecipitation (IP) of endogenous KAP1 from U2OS cells over-expressing wild-type (WT) HA-tagged ZNF354A or the indicated KAP-1 binding mutants left untreated or treated with 10□ng/ml of proaerolysin (toxin) at 37□°C, washed, and further incubated at 37□°C for 8 h. Blots show IP-fractions with Co-immunoprecipitated proteins (CoIP) and total cell extracts (TCE). **D.F** U2OS cells overexpressing ZNF354A WT or KRAB binding deficient mutant treated ± ferrostatin-1 (15 µM) at time 0 and 48 h post-transfection. **D.** Western blot analysis of TCEs showing levels of ZNF354A-HA and GAPDH throughout the experiment. **E-F.** Cell viability was monitored by ATP detection using Promega Glow in U2OS cells expressing an **E.** empty plasmid or **F.** cells overexpressing ZNF354A WT or KRAB binding deficient mutant. Cells were treated or not with ferrostatin-1 (15 µM) single treatment at time 0 (magenta). Results normalized to untreated controls expressing empty plasmid, (used for Fig 7F), set as 100%, are mean ± SD from one representative assay, of three (n = 35). *P*-values, (untreated controls vs. Fer-1 each timepoint), were obtained using two-way ANOVA with Sidak's correction.

Discussion

This study uncovers the LORD (Lipid Oxygen Radical Defense) pathway, an epigenetically controlled stress response route that protects cells against the harmful accumulation of membrane lipid peroxides. LORD is pivotal for detoxifying oxidized lipids, preserving membrane integrity, and modulating cellular susceptibility to ferroptosis.

Under normal conditions, many antioxidant defense genes, but not all, are repressed by the transcriptional regulator ZNF354A, which we identified as a master regulator of the expression of genes involved in lipid damage repair. ZNF354A was first identified as Kid-1 a C2H2 zinc finger transcription factor predominantly expressed in the kidney with its expression regulated during development and decreasing after injury [84–86]. As with most KZFPs, ZNF354A binds the global epigenetic regulator KAP1 thereby recruiting the SETDB1 H3K9 methyltransferase. A key non-canonical component of the LORD repressive complex is the transcriptional activator ATF2. Upon lipid peroxide accumulation, ATF2, along with KAP1 and ZNF354A, undergoes phosphorylation in a p38- and JNK-dependent manner. Phosphorylation of each of the three components is both necessary and sufficient for activation of the LORD pathway, as they induce the p38 and JNK-dependent phosphorylation of the others. It will be of great interest to understand the mechanisms that mediate this triple phosphorylation and why all three are required. This level of control already suggests that excessive activation of the LORD pathway could be harmful in certain physiological contexts, as is repression of the pathway (Fig. 7E).

Phosphorylation leads to the dissociation of ATF2-KAP1-SETBD1 from ZNF354A, which *in turn* detaches from the specific DNA loci, allowing the expression of genes involved in antioxidant defenses, protection against ferroptosis and possibly also other forms of cell death. Our findings reinforce the emerging role of KZFP-mediated regulatory circuits in orchestrating gene networks across diverse biological processes[35,36,60,87–89]. We reveal that additional factors, such as ATF2 can modulate KAP1-KZFP repression complexes in a pathway-specific manner.

Subsequent transcription of the ZNF354A silenced genes involves additional transcription factors. For *ZDHHC20L* expression, we found the requirement for ATF2 and three other transcription factors, FOXA1, SP1 and NRF2, the latter being well known to control antioxidant genes. Future studies will aim to uncover the complete network of transcription factors orchestrating the LORD-regulated genes.

Interestingly not all anti-oxidant genes are controlled by the LORD pathway. In particular, *GPX4* is not. Remarkably, however, during the writing of the current manuscript, GPX4 was reported to undergo ZDHHC20-mediated S-acylation, in a manner that regulates its activity[40], consistent with our unpublished data. Thus, while the expression of GPX4 is not controlled by the LORD pathway, its activity is, both through its acylation and the availability of GSH.

Identification of the LORD pathway offers promising therapeutic opportunities, whether through promoting ferroptosis to target cancer cells or inhibiting ferroptosis to protect against neurodegenerative and inflammatory diseases.

Acknowledgments

We warmly thank Dr. Martina Begnis, Dr. Julien Duc, Dr. Priscilla Turelli and Prof. Giovanni D'Angelo for helpful discussions throughout the study and comments on the manuscript. This work is supported by a generous foundation represented by CARIGEST SA, and SNF grant 310030_192608 to F.G. van der Goot.

Author contributions

Conceptualization, F.S.M., L.A., R.F., D.T., and F.G.v.d.G.; investigation, F.S.M., L.A., R.F., B.K., C.R., L.B., F.M., D.M., E.P., and O.R.; funding acquisition, F.G.v.d.G.; writing – original draft, F.S.M., L.A., R.F., D.T., and F.G.v.d.G.; writing – review & editing, F.S.M., L.A., R.F., L.B., F.M., D.M., O.R., D.T., and F.G.v.d.G.; resources, B.K. and C.R.

Declaration of Interest

The authors declare that a patent application related to the medical use of the findings reported in this study has been submitted.

Declaration of generative AI and AI-assisted technologies in the writing process

During the preparation of this work, the author(s) used ChatGPT in order to improve the language.

References

1. Lennicke, C., and Cochemé, H.M. (2021). Redox metabolism: ROS as specific molecular regulators of cell signaling and function. Molecular Cell *81*, 3691–3707. https://doi.org/10.1016/j.molcel.2021.08.018.

2. Sies, H., and Jones, D.P. (2020). Reactive oxygen species (ROS) as pleiotropic physiological signalling agents. Nat Rev Mol Cell Biol *21*, 363–383. https://doi.org/10.1038/s41580-020-0230-3.

3. Sies, H., Mailloux, R.J., and Jakob, U. (2024). Fundamentals of redox regulation in biology. Nat Rev Mol Cell Biol *25*, 701–719. https://doi.org/10.1038/s41580-024-00730-2.

4. Dixon, S.J., Lemberg, K.M., Lamprecht, M.R., Skouta, R., Zaitsev, E.M., Gleason, C.E., Patel, D.N., Bauer, A.J., Cantley, A.M., Yang, W.S., et al. (2012). Ferroptosis: An Iron-Dependent Form of Nonapoptotic Cell Death. Cell *149*, 1060–1072. https://doi.org/10.1016/j.cell.2012.03.042.

5. Qiu, B., Zandkarimi, F., Bezjian, C.T., Reznik, E., Soni, R.K., Gu, W., Jiang, X., and Stockwell, B.R. (2024). Phospholipids with two polyunsaturated fatty acyl tails promote ferroptosis. Cell *187*, 1177-1190.e18. https://doi.org/10.1016/j.cell.2024.01.030.

6. Yang, W.S., Kim, K.J., Gaschler, M.M., Patel, M., Shchepinov, M.S., and Stockwell, B.R. (2016). Peroxidation of polyunsaturated fatty acids by lipoxygenases drives ferroptosis. Proceedings of the National Academy of Sciences *113*, E4966–E4975. https://doi.org/10.1073/pnas.1603244113.

7. Dixon, S.J., and Olzmann, J.A. (2024). The cell biology of ferroptosis. Nat Rev Mol Cell Biol *25*, 424–442. https://doi.org/10.1038/s41580-024-00703-5.

8. Maher, P., Currais, A., and Schubert, D. (2020). Using the Oxytosis/Ferroptosis Pathway to Understand and Treat Age-Associated Neurodegenerative Diseases. Cell Chem Biol *27*, 1456–1471. https://doi.org/10.1016/j.chembiol.2020.10.010.

9. Stockwell, B.R., Friedmann Angeli, J.P., Bayir, H., Bush, A.I., Conrad, M., Dixon, S.J., Fulda, S., Gascón, S., Hatzios, S.K., Kagan, V.E., et al. (2017). Ferroptosis: A Regulated Cell Death Nexus Linking Metabolism, Redox Biology, and Disease. Cell *171*, 273–285. https://doi.org/10.1016/j.cell.2017.09.021.

10. Jiang, X., Stockwell, B.R., and Conrad, M. (2021). Ferroptosis: mechanisms, biology and role in disease. Nat Rev Mol Cell Biol *22*, 266–282. https://doi.org/10.1038/s41580-020-00324-8.

11. Stockwell, B.R. (2022). Ferroptosis turns 10: Emerging mechanisms, physiological functions, and therapeutic applications. Cell *185*, 2401–2421. https://doi.org/10.1016/j.cell.2022.06.003.

12. Conrad, M., and Proneth, B. (2020). Selenium: Tracing Another Essential Element of Ferroptotic Cell Death. Cell Chemical Biology *27*, 409–419. https://doi.org/10.1016/j.chembiol.2020.03.012.

13. Ingold, I., Berndt, C., Schmitt, S., Doll, S., Poschmann, G., Buday, K., Roveri, A., Peng, X., Porto Freitas, F., Seibt, T., et al. (2018). Selenium Utilization by GPX4 Is Required to Prevent Hydroperoxide-Induced Ferroptosis. Cell *172*, 409-422.e21. https://doi.org/10.1016/j.cell.2017.11.048.

14. Jose, E., March-Steinman, W., Wilson, B.A., Shanks, L., Parkinson, C., Alvarado-Cruz, I., Sweasy, J.B., and Paek, A.L. (2024). Temporal coordination of the transcription factor response to H2O2 stress. Nat Commun *15*, 3440. https://doi.org/10.1038/s41467-024-47837-w.

15. Anandhan, A., Dodson, M., Schmidlin, C.J., Liu, P., and Zhang, D.D. (2020). Breakdown of an Ironclad Defense System: The Critical Role of NRF2 in Mediating Ferroptosis. Cell Chem Biol *27*, 436–447. https://doi.org/10.1016/j.chembiol.2020.03.011.

16. Itoh, K., Chiba, T., Takahashi, S., Ishii, T., Igarashi, K., Katoh, Y., Oyake, T., Hayashi, N., Satoh, K., Hatayama, I., et al. (1997). An Nrf2/small Maf heterodimer mediates the induction of phase II detoxifying enzyme genes through antioxidant response elements. Biochem Biophys Res Commun *236*, 313–322. https://doi.org/10.1006/bbrc.1997.6943.

17. Kerins, M.J., and Ooi, A. (2018). The Roles of NRF2 in Modulating Cellular Iron Homeostasis. Antioxid Redox Signal *29*, 1756–1773. https://doi.org/10.1089/ars.2017.7176.

18. Raghunath, A., Sundarraj, K., Nagarajan, R., Arfuso, F., Bian, J., Kumar, A.P., Sethi, G., and Perumal, E. (2018). Antioxidant response elements: Discovery, classes, regulation and potential applications. Redox Biol *17*, 297–314. https://doi.org/10.1016/j.redox.2018.05.002.

19. Baird, L., and Yamamoto, M. (2020). The Molecular Mechanisms Regulating the KEAP1-NRF2 Pathway. Mol Cell Biol *40*, e00099-20. https://doi.org/10.1128/MCB.00099-20.

20. Koppula, P., Lei, G., Zhang, Y., Yan, Y., Mao, C., Kondiparthi, L., Shi, J., Liu, X., Horbath, A., Das, M., et al. (2022). A targetable CoQ-FSP1 axis drives ferroptosis- and radiation-resistance in KEAP1 inactive lung cancers. Nat Commun *13*, 2206. https://doi.org/10.1038/s41467-022-29905-1.

21. Bersuker, K., Hendricks, J.M., Li, Z., Magtanong, L., Ford, B., Tang, P.H., Roberts, M.A., Tong, B., Maimone, T.J., Zoncu, R., et al. (2019). The CoQ oxidoreductase FSP1 acts parallel to GPX4 to inhibit ferroptosis. Nature *575*, 688–692. https://doi.org/10.1038/s41586-019-1705-2.

22. Doll, S., Freitas, F.P., Shah, R., Aldrovandi, M., da Silva, M.C., Ingold, I., Goya Grocin, A., Xavier da Silva, T.N., Panzilius, E., Scheel, C.H., et al. (2019). FSP1 is a glutathione-independent ferroptosis suppressor. Nature *575*, 693–698. https://doi.org/10.1038/s41586-019-1707-0.

23. Habib, E., Linher-Melville, K., Lin, H.-X., and Singh, G. (2015). Expression of xCT and activity of system xc(-) are regulated by NRF2 in human breast cancer cells in response to oxidative stress. Redox Biol *5*, 33–42. https://doi.org/10.1016/j.redox.2015.03.003.

24. Sasaki, H., Sato, H., Kuriyama-Matsumura, K., Sato, K., Maebara, K., Wang, H., Tamba, M., Itoh, K., Yamamoto, M., and Bannai, S. (2002). Electrophile response element-mediated induction of the cystine/glutamate exchange transporter gene expression. J Biol Chem *277*, 44765–44771. https://doi.org/10.1074/jbc.M208704200.

25. Yang, W.S., SriRamaratnam, R., Welsch, M.E., Shimada, K., Skouta, R., Viswanathan, V.S., Cheah, J.H., Clemons, P.A., Shamji, A.F., Clish, C.B., et al. (2014). Regulation of ferroptotic cancer cell death by GPX4. Cell *156*, 317–331. https://doi.org/10.1016/j.cell.2013.12.010.

26. Forcina, G.C., Pope, L., Murray, M., Dong, W., Abu-Remaileh, M., Bertozzi, C.R., and Dixon, S.J. (2022). Ferroptosis regulation by the NGLY1/NFE2L1 pathway. Proc Natl Acad Sci U S A *119*, e2118646119. https://doi.org/10.1073/pnas.2118646119.

27. Chen, D., Fan, Z., Rauh, M., Buchfelder, M., Eyupoglu, I.Y., and Savaskan, N. (2017). ATF4 promotes angiogenesis and neuronal cell death and confers ferroptosis in a xCT-dependent manner. Oncogene *36*, 5593–5608. https://doi.org/10.1038/onc.2017.146.

28. Yang, W.-H., Ding, C.-K.C., Sun, T.A., Hsu, D.S., and Chi, J.-T. (2019). The Hippo Pathway Effector TAZ Regulates Ferroptosis in Renal Cell Carcinoma. Cell Rep *28*, 2501-2508.e4. https://doi.org/10.1016/j.celrep.2019.07.107.

29. A, T., L, M., Kt, B.-R., Y, L., J, Y., Ld, A., and Sj, D. (2018). p53 Suppresses Metabolic Stress-Induced Ferroptosis in Cancer Cells. Cell reports *22*. https://doi.org/10.1016/j.celrep.2017.12.077.

30. Yao, F., Deng, Y., Zhao, Y., Mei, Y., Zhang, Y., Liu, X., Martinez, C., Su, X., Rosato, R.R., Teng, H., et al. (2021). A targetable LIFR−NF-κB−LCN2 axis controls liver tumorigenesis and vulnerability to ferroptosis. Nat Commun *12*, 7333. https://doi.org/10.1038/s41467-021-27452-9.

31. Gao, R., Kalathur, R.K.R., Coto□Llerena, M., Ercan, C., Buechel, D., Shuang, S., Piscuoglio, S., Dill, M.T., Camargo, F.D., Christofori, G., et al. (2021). YAP/TAZ and ATF4 drive resistance to Sorafenib in hepatocellular carcinoma by preventing ferroptosis. EMBO Molecular Medicine *13*, e14351. https://doi.org/10.15252/emmm.202114351.

32. Wang, Y., Yang, L., Zhang, X., Cui, W., Liu, Y., Sun, Q., He, Q., Zhao, S., Zhang, G., Wang, Y., et al. (2019). Epigenetic regulation of ferroptosis by H2B monoubiquitination and p53. EMBO reports *20*, e47563. https://doi.org/10.15252/embr.201847563.

33. Palma, F.R., Coelho, D.R., Pulakanti, K., Sakiyama, M.J., Huang, Y., Ogata, F.T., Danes, J.M., Meyer, A., Furdui, C.M., Spitz, D.R., et al. (2024). Histone H3.1 is a chromatin-embedded redox sensor triggered by tumor cells developing adaptive phenotypic plasticity and multidrug resistance. Cell Reports *43*. https://doi.org/10.1016/j.celrep.2024.113897.

34. Gantner, B.N., Palma, F.R., Kayzuka, C., Lacchini, R., Foltz, D.R., Backman, V., Kelleher, N., Shilatifard, A., and Bonini, M.G. (2024). Histone oxidation as a new mechanism of metabolic control over gene expression. Trends in Genetics *40*, 739–746. https://doi.org/10.1016/j.tig.2024.05.012.

35. Imbeault, M., Helleboid, P.-Y., and Trono, D. (2017). KRAB zinc-finger proteins contribute to the evolution of gene regulatory networks. Nature *543*, 550–554. https://doi.org/10.1038/nature21683.

36. Rosspopoff, O., and Trono, D. (2023). Take a walk on the KRAB side. Trends in Genetics *39*, 844–857. https://doi.org/10.1016/j.tig.2023.08.003.

37. S. Mesquita, F., Abrami, L., Bracq, L., Panyain, N., Mercier, V., Kunz, B., Chuat, A., Carlevaro-Fita, J., Trono, D., and van der Goot, F.G. (2023). SARS-CoV-2 hijacks a cell damage response, which induces transcription of a more efficient Spike S-acyltransferase. Nat Commun *14*, 7302. https://doi.org/10.1038/s41467-023-43027-2.

38. Mesquita, F.S., Abrami, L., Sergeeva, O., Turelli, P., Qing, E., Kunz, B., Raclot, C., Paz Montoya, J., Abriata, L.A., Gallagher, T., et al. (2021). S-acylation controls SARS-CoV-2 membrane lipid organization and enhances infectivity. Developmental Cell *56*, 2790-2807.e8. https://doi.org/10.1016/j.devcel.2021.09.016.

39. López-Otín, C., Blasco, M.A., Partridge, L., Serrano, M., and Kroemer, G. (2023). Hallmarks of aging: An expanding universe. Cell *186*, 243–278. https://doi.org/10.1016/j.cell.2022.11.001.

40. Huang, B., Wang, H., Liu, S., Hao, M., Luo, D., Zhou, Y., Huang, Y., Nian, Y., Zhang, L., Chu, B., et al. (2025). Palmitoylation-dependent regulation of GPX4 suppresses ferroptosis. Nat Commun *16*, 867. https://doi.org/10.1038/s41467-025-56344-5.

41. ENCODE Project Consortium (2012). An integrated encyclopedia of DNA elements in the human genome. Nature *489*, 57–74. https://doi.org/10.1038/nature11247.

42. Luo, Y., Hitz, B.C., Gabdank, I., Hilton, J.A., Kagda, M.S., Lam, B., Myers, Z., Sud, P., Jou, J., Lin, K., et al. (2020). New developments on the Encyclopedia of DNA Elements (ENCODE) data portal. Nucleic Acids Res *48*, D882–D889. https://doi.org/10.1093/nar/gkz1062.

43. Haeussler, M., Zweig, A.S., Tyner, C., Speir, M.L., Rosenbloom, K.R., Raney, B.J., Lee, C.M., Lee, B.T., Hinrichs, A.S., Gonzalez, J.N., et al. (2019). The UCSC Genome Browser database: 2019 update. Nucleic Acids Research *47*, D853–D858. https://doi.org/10.1093/nar/gky1095.

44. van Dam, H., Wilhelm, D., Herr, I., Steffen, A., Herrlich, P., and Angel, P. (1995). ATF-2 is preferentially activated by stress-activated protein kinases to mediate c-jun induction in response to genotoxic agents. EMBO J *14*, 1798–1811. https://doi.org/10.1002/j.1460-2075.1995.tb07168.x.

45. Bhoumik, A., Takahashi, S., Breitweiser, W., Shiloh, Y., Jones, N., and Ronai, Z. (2005). ATM-Dependent Phosphorylation of ATF2 Is Required for the DNA Damage Response. Molecular Cell *18*, 577–587. https://doi.org/10.1016/j.molcel.2005.04.015.

46. Gupta, S., Campbell, D., Dérijard, B., and Davis, R.J. (1995). Transcription Factor ATF2 Regulation by the JNK Signal Transduction Pathway. Science *267*, 389–393. https://doi.org/10.1126/science.7824938.

47. Kirsch, K., Zeke, A., Tőke, O., Sok, P., Sethi, A., Sebő, A., Kumar, G.S., Egri, P., Póti, Á.L., Gooley, P., et al. (2020). Co-regulation of the transcription controlling ATF2 phosphoswitch by JNK and p38. Nat Commun *11*, 5769. https://doi.org/10.1038/s41467-020-19582-3.

48. Yamasaki, T., Takahashi, A., Pan, J., Yamaguchi, N., and Yokoyama, K.K. (2009). Phosphorylation of Activation Transcription Factor-2 at Serine 121 by Protein Kinase C Controls c-Jun-mediated Activation of Transcription. J Biol Chem *284*, 8567–8581. https://doi.org/10.1074/jbc.M808719200.

49. Sakurai, A., Maekawa, T., Sudo, T., Ishii, S., and Kishimoto, A. (1991). Phosphorylation of cAMP response element-binding protein, CRE-BP1, by cAMP-dependent protein kinase and protein kinase C. Biochemical and Biophysical Research Communications *181*, 629–635. https://doi.org/10.1016/0006-291X(91)91237-7.

50. Lau, E., and Ronai, Z.A. (2012). ATF2 – at the crossroad of nuclear and cytosolic functions. Journal of Cell Science *125*, 2815–2824. https://doi.org/10.1242/jcs.095000.

51. Watson, G., Ronai, Z., and Lau, E. (2017). ATF2, a paradigm of the multifaceted regulation of transcription factors in biology and disease. Pharmacol Res *119*, 347–357. https://doi.org/10.1016/j.phrs.2017.02.004.

52. Lopez-Bergami, P., Lau, E., and Ronai, Z. (2010). Emerging roles of ATF2 and the dynamic AP1 network in cancer. Nat Rev Cancer *10*, 65–76. https://doi.org/10.1038/nrc2681.

53. Bischofberger, M., Iacovache, I., and van der Goot, F.G. (2012). Pathogenic pore-forming proteins: function and host response. Cell Host Microbe *12*, 266–275. https://doi.org/10.1016/j.chom.2012.08.005.

54. Brito, C., Cabanes, D., Sarmento Mesquita, F., and Sousa, S. (2019). Mechanisms protecting host cells against bacterial pore-forming toxins. Cell. Mol. Life Sci. *76*, 1319–1339. https://doi.org/10.1007/s00018-018-2992-8.

55. Schultz, D.C., Ayyanathan, K., Negorev, D., Maul, G.G., and Rauscher, F.J. (2002). SETDB1: a novel KAP-1-associated histone H3, lysine 9-specific methyltransferase that contributes to HP1-mediated silencing of euchromatic genes by KRAB zinc-finger proteins. Genes Dev *16*, 919–932. https://doi.org/10.1101/gad.973302.

56. Iyengar, S., and Farnham, P.J. (2011). KAP1 Protein: An Enigmatic Master Regulator of the Genome. J Biol Chem *286*, 26267–26276. https://doi.org/10.1074/jbc.R111.252569.

57. Iglesias, N., and Moazed, D. (2017). Silencing repetitive DNA. eLife *6*, e29503. https://doi.org/10.7554/eLife.29503.

58. O'Geen, H., Squazzo, S.L., Iyengar, S., Blahnik, K., Rinn, J.L., Chang, H.Y., Green, R., and Farnham, P.J. (2007). Genome-Wide Analysis of KAP1 Binding Suggests Autoregulation of KRAB-ZNFs. PLOS Genetics *3*, e89. https://doi.org/10.1371/journal.pgen.0030089.

59. de Tribolet-Hardy, J., Thorball, C.W., Forey, R., Planet, E., Duc, J., Coudray, A., Khubieh, B., Offner, S., Pulver, C., Fellay, J., et al. (2023). Genetic features and genomic targets of human KRAB-zinc finger proteins. Genome Res *33*, 1409–1423. https://doi.org/10.1101/gr.277722.123.

60. Helleboid, P.-Y., Heusel, M., Duc, J., Piot, C., Thorball, C.W., Coluccio, A., Pontis, J., Imbeault, M., Turelli, P., Aebersold, R., et al. (2019). The interactome of KRAB zinc finger proteins reveals the evolutionary history of their functional diversification. The EMBO Journal *38*. https://doi.org/10.15252/embj.2018101220.

61. Stoll, G.A., Pandiloski, N., Douse, C.H., and Modis, Y. (2022). Structure and functional mapping of the KRAB□KAP1 repressor complex. EMBO J *41*, e111179. https://doi.org/10.15252/embj.2022111179.

62. Li, X., Lee, Y.-K., Jeng, J.-C., Yen, Y., Schultz, D.C., Shih, H.-M., and Ann, D.K. (2007). Role for KAP1 serine 824 phosphorylation and sumoylation/desumoylation switch in regulating KAP1-mediated transcriptional repression. J Biol Chem *282*, 36177–36189. https://doi.org/10.1074/jbc.M706912200.

63. Bolderson, E., Savage, K.I., Mahen, R., Pisupati, V., Graham, M.E., Richard, D.J., Robinson, P.J., Venkitaraman, A.R., and Khanna, K.K. (2012). Kruppel-associated Box (KRAB)-associated co-repressor (KAP-1) Ser-473 phosphorylation regulates heterochromatin protein 1β (HP1-β) mobilization and DNA repair in heterochromatin. J Biol Chem *287*, 28122–28131. https://doi.org/10.1074/jbc.M112.368381.

64. Hu, C., Zhang, S., Gao, X., Gao, X., Xu, X., Lv, Y., Zhang, Y., Zhu, Z., Zhang, C., Li, Q., et al. (2012). Roles of Kruppel-associated Box (KRAB)-associated Co-repressor KAP1 Ser-473 Phosphorylation in DNA Damage Response. J Biol Chem *287*, 18937–18952. https://doi.org/10.1074/jbc.M111.313262.

65. Jang, S.M., Kauzlaric, A., Quivy, J.-P., Pontis, J., Rauwel, B., Coluccio, A., Offner, S., Duc, J., Turelli, P., Almouzni, G., et al. (2018). KAP1 facilitates reinstatement of heterochromatin after DNA replication. Nucleic Acids Research *46*, 8788–8802. https://doi.org/10.1093/nar/gky580.

66. White, D.E., Rafalska-Metcalf, I.U., Ivanov, A.V., Corsinotti, A., Peng, H., Lee, S.C., Trono, D., Janicki, S.M., and Rauscher, F.J. (2012). The ATM substrate KAP1 controls DNA repair in heterochromatin: Regulation by HP1 proteins and Serine 473/824 phosphorylation. Mol Cancer Res *10*, 401–414. https://doi.org/10.1158/1541-7786.MCR-11-0134.

67. Cheng, C.-T., Kuo, C.-Y., Ouyang, C., Li, C.-F., Chung, Y., Chan, D.C., Kung, H.-J., and Ann, D.K. (2016). Metabolic Stress-Induced Phosphorylation of KAP1 Ser473 Blocks Mitochondrial Fusion in Breast Cancer Cells. Cancer Research *76*, 5006–5018. https://doi.org/10.1158/0008-5472.CAN-15-2921.

68. Mertins, P., Mani, D.R., Ruggles, K.V., Gillette, M.A., Clauser, K.R., Wang, P., Wang, X., Qiao, J.W., Cao, S., Petralia, F., et al. (2016). Proteogenomics connects somatic mutations to signalling in breast cancer. Nature *534*, 55–62. https://doi.org/10.1038/nature18003.

69. Wu, F., Wang, P., Zhang, J., Young, L.C., Lai, R., and Li, L. (2010). Studies of Phosphoproteomic Changes Induced by Nucleophosmin-Anaplastic Lymphoma Kinase (ALK) Highlight Deregulation of Tumor Necrosis Factor (TNF)/Fas/TNF-related Apoptosis-induced Ligand Signaling Pathway in ALK-positive Anaplastic Large Cell Lymphoma. Mol Cell Proteomics *9*, 1616–1632. https://doi.org/10.1074/mcp.M000153-MCP201.

70. Krischuns, T., Günl, F., Henschel, L., Binder, M., Willemsen, J., Schloer, S., Rescher, U., Gerlt, V., Zimmer, G., Nordhoff, C., et al. (2018). Phosphorylation of TRIM28 Enhances the Expression of IFN-β and Proinflammatory Cytokines During HPAIV Infection of Human Lung Epithelial Cells. Front Immunol *9*, 2229. https://doi.org/10.3389/fimmu.2018.02229.

71. Ludwig, S., Ehrhardt, C., Neumeier, E.R., Kracht, M., Rapp, U.R., and Pleschka, S. (2001). Influenza Virus-induced AP-1-dependent Gene Expression Requires Activation of the JNK Signaling Pathway *. Journal of Biological Chemistry *276*, 10990–10998. https://doi.org/10.1074/jbc.M009902200.

72. Lozano-Sepulveda, S.A., Bautista-Osorio, E., Merino-Mascorro, J.A., Varela-Rey, M., Muñoz-Espinosa, L.E., Cordero-Perez, P., Martinez-Chantar, M.L., and Rivas-Estilla, A.M. (2016). S-adenosyl-L-methionine modifies antioxidant-enzymes, glutathione-biosynthesis and methionine adenosyltransferases-1/2 in hepatitis C virus-expressing cells. World J Gastroenterol *22*, 3746–3757. https://doi.org/10.3748/wjg.v22.i14.3746.

73. Koppula, P., Zhuang, L., and Gan, B. (2021). Cystine transporter SLC7A11/xCT in cancer: ferroptosis, nutrient dependency, and cancer therapy. Protein Cell *12*, 599–620. https://doi.org/10.1007/s13238-020-00789-5.

74. Mandal, P.K., Seiler, A., Perisic, T., Kölle, P., Banjac Canak, A., Förster, H., Weiss, N., Kremmer, E., Lieberman, M.W., Bannai, S., et al. (2010). System xc− and Thioredoxin Reductase 1 Cooperatively Rescue Glutathione Deficiency. J Biol Chem *285*, 22244–22253. https://doi.org/10.1074/jbc.M110.121327.

75. Labunskyy, V.M., Hatfield, D.L., and Gladyshev, V.N. (2014). Selenoproteins: Molecular Pathways and Physiological Roles. Physiol Rev *94*, 739–777. https://doi.org/10.1152/physrev.00039.2013.

76. Conrad, M., Lorenz, S.M., and Proneth, B. (2021). Targeting Ferroptosis: New Hope for As-Yet-Incurable Diseases. Trends Mol Med *27*, 113–122. https://doi.org/10.1016/j.molmed.2020.08.010.

77. Gaschler, M.M., and Stockwell, B.R. (2017). Lipid peroxidation in cell death. Biochemical and biophysical research communications *482*, 419. https://doi.org/10.1016/j.bbrc.2016.10.086.

78. Dixon, S.J., Patel, D.N., Welsch, M., Skouta, R., Lee, E.D., Hayano, M., Thomas, A.G., Gleason, C.E., Tatonetti, N.P., Slusher, B.S., et al. (2014). Pharmacological inhibition of cystine–glutamate exchange induces endoplasmic reticulum stress and ferroptosis. eLife *3*, e02523. https://doi.org/10.7554/eLife.02523.

79. Zilka, O., Shah, R., Li, B., Friedmann Angeli, J.P., Griesser, M., Conrad, M., and Pratt, D.A. (2017). On the Mechanism of Cytoprotection by Ferrostatin-1 and Liproxstatin-1 and the Role of Lipid Peroxidation in Ferroptotic Cell Death. ACS Cent. Sci. *3*, 232–243. https://doi.org/10.1021/acscentsci.7b00028.

80. Yamanaka, K., Saito, Y., Sakiyama, J., Ohuchi, Y., Oseto, F., and Noguchi, N. (2012). A novel fluorescent probe with high sensitivity and selective detection of lipid hydroperoxides in cells. RSC Adv. *2*, 7894–7900. https://doi.org/10.1039/C2RA20816D.

81. Li, B., and Pratt, D.A. (2015). Methods for determining the efficacy of radical-trapping antioxidants. Free Radical Biology and Medicine *82*, 187–202. https://doi.org/10.1016/j.freeradbiomed.2015.01.020.

82. Tycko, J., DelRosso, N., Hess, G.T., Aradhana, null, Banerjee, A., Mukund, A., Van, M.V., Ego, B.K., Yao, D., Spees, K., et al. (2020). High-Throughput Discovery and Characterization of Human Transcriptional Effectors. Cell *183*, 2020-2035.e16. https://doi.org/10.1016/j.cell.2020.11.024.

83. Wang, W., Cai, J., Wu, Y., Hu, L., Chen, Z., Hu, J., Chen, Z., Li, W., Guo, M., and Huang, Z. (2013). Novel activity of KRAB domain that functions to reinforce nuclear localization of KRAB-containing zinc finger proteins by interacting with KAP1. Cell. Mol. Life Sci. *70*, 3947–3958. https://doi.org/10.1007/s00018-013-1359-4.

84. Witzgall, R., O'Leary, E., Gessner, R., Ouellette, A.J., and Bonventre, J.V. (1993). Kid-1, a putative renal transcription factor: regulation during ontogeny and in response to ischemia and toxic injury. Mol Cell Biol *13*, 1933–1942. https://doi.org/10.1128/mcb.13.3.1933-1942.1993.

85. Witzgall, R., Volk, R., Yeung, R.S., and Bonventre, J.V. (1994). Genomic structure and chromosomal location of the rat gene encoding the zinc finger transcription factor Kid-1. Genomics *20*, 203–209. https://doi.org/10.1006/geno.1994.1154.

86. Shakib, K., Norman, J.T., Fine, L.G., Brown, L.R., and Godovac-Zimmermann, J. (2005). Proteomics profiling of nuclear proteins for kidney fibroblasts suggests hypoxia, meiosis, and cancer may meet in the nucleus. PROTEOMICS *5*, 2819–2838. https://doi.org/10.1002/pmic.200401108.

87. Begnis, M., Duc, J., Offner, S., Grun, D., Sheppard, S., Rosspopoff, O., and Trono, D. (2024). Clusters of lineage-specific genes are anchored by ZNF274 in repressive perinucleolar compartments. Science Advances *10*, eado1662. https://doi.org/10.1126/sciadv.ado1662.

88. Martins, F., Rosspopoff, O., Carlevaro-Fita, J., Forey, R., Offner, S., Planet, E., Pulver, C., Pak, H., Huber, F., Michaux, J., et al. (2024). A Cluster of Evolutionarily Recent KRAB Zinc Finger Proteins Protects Cancer Cells from Replicative Stress–Induced Inflammation. Cancer Research *84*, 808–826. https://doi.org/10.1158/0008-5472.CAN-23-1237.

89. Pontis, J., Planet, E., Offner, S., Turelli, P., Duc, J., Coudray, A., Theunissen, T.W., Jaenisch, R., and Trono, D. (2019). Hominoid-Specific Transposable Elements and KZFPs Facilitate Human Embryonic Genome Activation and Control Transcription in Naive Human ESCs. Cell Stem Cell *24*, 724-735.e5. https://doi.org/10.1016/j.stem.2019.03.012.

90. McLean, C.Y., Bristor, D., Hiller, M., Clarke, S.L., Schaar, B.T., Lowe, C.B., Wenger, A.M., and Bejerano, G. (2010). GREAT improves functional interpretation of cis-regulatory regions. Nat Biotechnol *28*, 495–501. https://doi.org/10.1038/nbt.1630.

91. Quinlan, A.R., and Hall, I.M. (2010). BEDTools: a flexible suite of utilities for comparing genomic features. Bioinformatics *26*, 841–842. https://doi.org/10.1093/bioinformatics/btq033.

92. Benjamini, Y., and Hochberg, Y. (1995). Controlling the False Discovery Rate: A Practical and Powerful Approach to Multiple Testing. Journal of the Royal Statistical Society. Series B (Methodological) *57*, 289–300.

STAR Methods

Resource availability

All resources and materials will be made available upon reasonable request to Gisou van der Goot (gisou.vandergoot@epfl.ch).

Materials availability

All data supporting the findings of this study are available within the paper, and the Supplementary Information. All data regarding the human *ZDHHC20* locus was obtained from the Genome browser on Human (GRCh37/hg19) (version hg19); Transcript data obtained from GENCODE Genes track (V4 0lift37) https://genome.ucsc.edu/cgi-bin/hgTrackUi?g=knownGene; Transcription factor binding sites and Chromatin State segmentation obtained from ENCODE https://genome.ucsc.edu/cgi-bin/hgTrackUi?db=hg18&g=wgEncodeBroadHmm and https://genome.ucsc.edu/cgi-bin/hgTrackUi?hgsid=2468617405_fC2FHA661Zobf2VQ1vQVBSTt1M4b&c=chr5&g=wgEncodeReg. Available KZFP ChIP-seq data was obtained from https://tronoapps.epfl.ch/web/krabopedia/

Cell lines

U2OS (ATCC: HTB_96), MDA-MB-231 (ATCC: HTB_26), K-562 (ATCC: CCL_243), SUDHL4 (ATCC: CRL_2957), SUDHL5 (ATCC: CRL_2958), SUDHL6 (ATCC: CRL_2959), MCF7 (ATCC: HTB_22), SW480 (ATCC: CCL_228), LS1034 (ATCC: CRL_2158), HCT116 (ATCC: CRL_3502), HAP-1 (Horizon Discovery: HZGGHC9001), HAP-1 KO_KAP1 (Horizon Discovery: HZGHC000293c003), HEPG2 (ATCC: HB_8065), Calu-3 (ATCC: HTB_55), 3T3 (ATCC: CRL_1658), VERO-E6 (ATCC: CRL_1586) cells

were grown in Dulbecco's Modified Eagle Medium supplemented with 10% FBS, penicillin, and streptomycin. HELA (ATCC: CCL_2) cells were grown in MEM Media supplemented with 10% fetal calf serum, 1% penicillin–streptomycin, 1% NEAA and 1% glutamine (all media from ThermoFisher Scientific).

Antibodies and Reagents

The antibodies and reagents were acquired from: ATF2 (Abcam: ab_131484; RRID: AB_11156678, rabbit: 1:2000x), phosphor-ATF2 (T69) (Abcam : 131106; RRID: AB_11157608;rabbit:1:1000x), GAPDH (Thermofisher : 398600; RRID: AB_2533438; mouse: 1:4000x), ZDHHC20 (Sigma: SAB4501054; RRID: AB_10744838; rabbit: 1:2000x), HA-HRP (Roche: 112013819001; RRID: AB_390917; rat: 1:5000x), KAP1 (Abcam: ab_109289; RRID: AB_10863057, rabbit: 1:1000x), phosphor-KAP1 S473 was generated in D. TRONO laboratory using the following peptide krsrSgegevsgl (rabbit: 1:500x), Nucleocapside N SARS-CoV-2 (Genetex: GTX135357; RRID: AB_2868464; rabbit 1:4000x), FLAG (Sigma: F3165; RRID: AB_259529; mouse: 1:2000x), phosphor-Threonine-Serine (BD: 612548; RRID: AB_399843; rabbit: 1:1000x), GPX4 (Cell Signalling: 52455; RRID: AB_2924984, rabbit: 1:1000x), SETDB1 (Novus Biologicals: NBP1_51677; RRID: AB_11002952, mouse: 1:2000x), NRF2 (Abnova: H00004780; RRID:566020, mouse: 1:2000x), V5-HRP (Sigma: V2260; RRID: AB_261857, mouse : 1:2000x), Actin (Millipore: MAB1501; RRID: AB_2223041, mouse: 1:4000x), MAT1A (Abcam: 129176; RRID: AB_11145300, rabit: 1:2000x), ZNF354A (Santa Cruz: 81140; RRID: AB_1131557, mouse: 1:1000x), 4G10 phospho-Tyrosine (Millipore: 05-321; RRID: AB_309678, mouse: 1:1000x) and HRP-conjugated secondary antibodies (GE-Healthcare).

RSL-3 (Sigma: S8155), Hydrogen Peroxide 30% (Fisher: H/1750/15), Rotenone (Cayman Chemical: CAY-13995), Ferrostatin-1 (Sigma: SML0583), Bodipy 581/591 C11 (Sigma: D3861), Liperfluo (Fisher: L248), Propidium Iodide (Thermofisher: P3566), Cell Viability assay (Promega: G9711), JQ1 (Sigma: SML-1524), Mithramycin (LKT: M3476), Erastin

(Millipore: 329600) , all resuspended in DMSO and N-acetylcysteine (Selleckchem: S1623) resuspended in water, with pH adjusted to 7.4).

siRNA

For human ZNF354A, 3 different siRNA in 3'-UTR were tested and validated, from Qiagen: ZNF354A (TACATCCTTGAGAGAGATGTA), from Santa Cruz (sc-91974), ZNF354A **(**GTCACGTGATCATCAGAAA), and from Origene , ZNF354A (GAGGTTTATCCATGGAATTAAATACCT).

The other following human siRNA with the corresponding target sequences were purchased from Qiagen : ZNF 317 (CATGACGGAAATCACACTAAA), ZNF 308 (CAGTTCATTGGCAACCTCATA), ZNF 677 (GAGATTGGTTACAGTACAAGA), ZNF793 (ACCCTGGCATGTAAACGTTTA), SETDB1 (TCGGGTGGTCGCCAAATACAA), KAP1 (AGCGTCCTGGCACTAACTCAA), ATF2 (CCGAGGTAGTCCACATACAGAA), NRF2/NFE2L2 (CCCATTGATCTTTCTGATCTA), GPX4 (CGGCTGCGTGGTGAAGCGCTA). The following human siRNA were purchased from Santa Cruz: SP1 (sc-44221), FOXA1 (sc-37930). Mouse siRNA were purchased from Qiagen for mouse ZFP354A (TACCACTTTAATAACATTCAA). As a control siRNA, a sequence targeting the viral glycoprotein VSV-G (5'-ATTGAACAAACGAAACAAGGA-3') was used. Transfections of 50 nM of siRNA were carried out using *TRANS*IT-X2 (MIRUS), and the cells were analyzed at least 72 h after transfection.

Western Blotting

Cells were washed three times in 1x PBS at 4°C and lysed in Buffer (1x PBS, 0.5% NP40 and protease inhibitor cocktail; Roche) for 30 min on ice. Lysates were then spin down at 10 000 g, and the protein content of supernatant were determined, the samples were boiled in Laemmli buffer for 5 min before separation via SDS-PAGE and western blotting against the different anti-bodies used in this study. For the analysis of phosphorylated proteins, SuperSep™ Phos-tag™ gels (cat. no. 199-18011) were used. Western blots were developed

using the ECL protocol and imaged on a Fusion Solo from Vilber Lourmat. Densitometric analysis was performed using the software Bio-1D from the manufacturer.

Plasmids

Plasmids expressing HA-tagged ZNF354A-HA, ZNF317-HA, ZNF677-HA, ZNF793-HA, KAP1-HA were obtained from the D. Trono lab [35]. Plasmids expressing FLAG-ATF2 were from Origene (RC2118983), myc-SETDB1 (RC2266620) and plasmids expressing SP1-FLAG (25543) and FOXA1-V5 (153109) from Addgene. Mutations to change KAP1-HA to KAP1-FLAG, ZNF354A-HA to ZNF354A-FLAG, FLAG-ATF2 to HA-ATF2, HA-ATF2 6A (T52A-T69A-T71A-T73A-S490A-S498A), HA-ATF2 6D (T52D-T69D-T71D-T73D-S490D-S498D), ZNF354A-HA (S169A), ZNF354A-HA (S169D), ZNF354A-HA (T189A), ZNF354A (T154A), ZNF354A-HA RR (D18R-E27R), ZNF354A RA (E45R-N46A), ZNF354A RR-RA (D18R-E27R- E45R-N46A), KAP1-HA (S473A), KAP1-HA (S473D) and MYC-SETDB1 inactive form (H1224A-C1226A-C1279A-C1280A-C1281A) were done following Quickchange mutagenesis kit (Agilent) instructions.

Oligonucleotides for Quantitative RT-PCR

All QPCR primers, used in this study are described in detail in table below (Table S1).

Primers	**Forward**	**Reverse**
ALAS-1	CTCACCACACACCCCAGATG	AGTTCCAGCCCCACTTGCT
ATF2	AGTCTGATTGGCTTAACTCGTATT	CACAGGTCCTTGTATTGCCTG
FSP1	ACAGAATATCCTGAGAAAGAGGTCA	ATCTCCTTCACTTCCTGC
GLRX	AACAGAGTGGGGAACTGCTG	AACATTTCCTATGAGATCTGTGGTT

GPX4	GCATCCTGGGAAATGCCATC	GGAGAGACGGTGTCCAAACT
GUSS	CCACCAGGGACCATCCAAT	AGTCAAAATATGTGTTCTGGACAAAGTAA
MAT1A	GGGACACCCGGATAAGATC	CACCACACAGCAGCACCATG
SELB	CCTTGTGATCGGCCAGATTG	TGTTCTCTAGGGTCTTCTGCATT
SELS	CTTTGCGGGGAGGAGGTTA	AGGGTTCATCTTGCTAATGTCAA
SEPHS2	CCTGTCACTGGTGCAGACCAC	CCCATGGCGTAGAGGTCACTC
SEPP1	CTGTGGCTTTGTGGAGCTG	ACATTGCTGGGGTTGTCCTAT
SEPSECS	GCTGTCATGAACCGCGAG	GGACACTTGCCCTTCTCCA
SLC7A11	TGCATATGCTGGCTGGTTTT	GGCCACATTTGTCAGCACAT
TBP	GCCCGAAACGCCGAATATA	CGTGGCTCTCTTATCCTCATGA
TXNRD3	TTCATGTGCGAAGGAAGCT	GGTGACGGGACAACAAAGTC
TXRND1	AAAGGCAAGAACGGCGATG	CAGGGTGATGATCTTTAGCTGAC
ZDHHC20 1	GTGGCCTTATTTGGAAGTGGG	CCCTACTCTAGTATGGCCTC
ZDHHC20 2	GCCACTGCCACTGCAGGTC	CACAGCCATGTGCCCTCTG
ZDHHC20 3	GGCACAAAATCAGGGAGAACAG	AAGAAGACGTCACCCTTTGCT
ZDHHC20 4	AGTCTCCCTCCCCTATTGAGT	AAAACACGCCCTTGATGGAT
ZDHHC20 5	CCTCGGACTTTTGCTCCCACAAG	CGTCCCACCGTTCTGGGGAG
ZDHHC20 C1	CGCCTTGTGGGGATGGATCC	CCGCTTGTTGGACAGTGAATCTCAG
ZDHHC20 C2	GTCGTCTGGTCCTACTACGC	AGCCACAAGGTAAACAACGG
ZNF354A	CGAGGCCCCAGGTGTC	TAAATGGGAGCCCCAGTGAG
NRF2	AACTACTCCCAGGTTGCCC	TACAAACGGGAATGTCTGCG
setdb1	GGCACATGGTGGAAGTCCCGAG	GCTGAACATGGGCTCCAGCCG
KAP1_TRIM28	AAGGACACTGTGCGCTCTAC	ACGTTGCAATAGACAGTACGTTCAC

Table S1 - Primers against human genes used in this study.

Aerolysin purification and cell intoxication

Proaerolysin toxin was produced and purified by our laboratory in Aeromonas salmonicida as previously described (ref). Cells were treated one hour in complete medium with 10 ng/ml of proaerolysin at 37 °C. Cells were washed twice in complete medium and further incubated at 37 °C for indicated times.

GREAT – analysis

ChIP-seq data for ZNF354A-HA binding sites were obtained from KRABopedia [59] and submitted to the Genomic Regions Enrichment of Annotations Tool (GREAT - http://great.stanford.edu/public/html/) [90]. The parameters for gene regulatory domains for each gene were defined as domain that extends in both directions of the TSS until the nearest TSS up to a maximum extension of 300 kb.

Human MucilAir assays

MucilAir-human upper respiratory tissues (Epithelix, Geneve, Switzerland) were maintained according to the manufacturer's protocol. For infection, tissues were washed apically with 200 µl of DPBS, calcium, magnesium (#14040091—Gibco) for 20 min at 37 °C and the basal medium replaced with fresh mucilair medium. Tissues were infected at the MOI of 0.1 PFU (assuming the manufacturer's estimations of 500000 cells per tissue). Tissues were inoculated with 200 µl of SARS-CoV-2 (passage 3) for 3 h (apically) at 33 °C. The apical inoculum was removed and infected tissues were maintained for until harvest. For harvest tissues were lysed using 300 µl lysis buffer for 30 min and processed for western blot.

Viral Stock production and titration with plaque-based assays

All viral stocks were produced and isolated from supernatants of Vero E6 cells, cultured in T75 culture flasks to a confluency of 80-90%, and infected with an original passage 2 (P2) SARS-CoV-2 virus, for 48 or 72 h, at MOI≈0.05, in 10 ml DMEM supplemented with 2.5% FCS. Original stocks were obtained from the following strain: hCoV-19/Switzerland/GE9586/2020|EPI_ISL_414022|2020-02-27. Passage 3 supernatants were harvested, clear of cell debris by centrifugation (500 *g* 10 min) and filtration (0.45 µm), aliquoted and stored at -80 C. Viral titers were quantified by determining the number of individual plaque forming units after 48 h of infection in confluent Vero E6 cells as described in [37].

SARS CoV-2 infections

All infections for experimental analysis were done using passage 3 SARS-CoV-2 stocks. Vero E6 cells or CALU-3 cells seeded to a confluency of 90 to 100%, were, washed twice in warm serum-free medium and inoculated with the indicated MOI of SARS-CoV-2, diluted in serum free medium. 1 hour after inoculation cells were washed with complete medium and infection allowed to proceed for the indicated time points in DMEM supplemented with 2.5% FCS, penicillin and streptomycin.

Drug and toxin treatments

All drug treatments were done for the indicated times in complete culture and/or infection medium. Equivalent volume of Dimethyl sulfoxide (DMSO), used as a solvent, was added for control samples. Specifically, culture media was replaced, cells were washed once in warm culture media and drugs resuspended as indicated were used as: RSL3 (in DMSO - 3 μM, increasing concentrations 0.6 to 10 μM), Ferrostatin-1 (DMSO - 1 – 15 μM), H□O□ (0.5 – 100 μM)**,** Rotenone (1 – 10 μM).

UCSC genome browser analysis

UCSC genome browser at ZDHHC20 locus was obtained from (Human version hg19). Specific UCSC genome browser tracks were selected for display in Fig. 1 and 2. Transcript annotation corresponds to GENCODE Genes track (version V4 0lift37); Histone Modifications by ChIP-seq from ENCODE/Stanford/Yale/USC/Harvard display ChIP-seq signals for H3K4me1, H3K4me3, H3K27Ac marks for HepG2 and H3K9me3 for U2OS. Transcription Factor CHIP-seq Peaks track shows transcription factor SETDB1, and KAP1binding sites for U2OS and K562 cells based on ChIP-seq experiments from ENCODE. KZFP CHIP-seq data show binding sites for different KZFP proteins obtained from KRABopedia (https://tronoapps.epfl.ch/web/krabopedia/) (https://doi.org/10.1101/2023.02.27.530095)

Q-RT-PCR

For the real-time PCR, RNA was extracted from a six-well dish using the RNeasy kit (Qiagen). In all, 0.5-1 mg of the total RNA extracted was used for the reverse transcription using random hexamers and superscript II (Invitrogen). A 1:40 dilution of the cDNA was used to perform the real-time PCR using using Applied Biosystems SYBR Green Master Mix on 7900 HT Fast QPCR System (Applied Biosystems) with SDS 2.4 Software. All data (always in triplicate) were normalized to Ct values from three housekeeping (HK) genes ALAS-1, Guss and TBP. Results were expressed as 2^(-ΔΔCt)*100%.

Chromatin Immunoprecipitation followed by qPCR (ChIP-qPCR) or sequencing.

K562 cells (30 million) were cross-linked at room temperature for 10 minutes by adding formaldehyde to a final concentration of 1%, followed by quenching with glycine Tris 200mM. Cells were washed twice with PBS, pelleted, and stored at -80°C. Pellets were sequentially lysed in LB1 (50 mM HEPES-KOH pH 7.4, 140 mM NaCl, 1 mM EDTA, 0.5 mM EGTA, 10% glycerol, 0.5% NP-40, 0.25% Triton X-100, protease inhibitors), LB2 (10 mM Tris-HCl pH 8.0, 200 mM NaCl, 1 mM EDTA, 0.5 mM EGTA, protease inhibitors), and SDS shearing buffer (10 mM Tris-HCl pH 8.0, 1 mM EDTA, SDS 0.15%, protease inhibitors) . Chromatin was sonicated (Covaris: 5% duty, 200 cycles, 140 PIP, 20 min 25min) to obtain DNA fragments of 100-300bp. ChIP was performed anti-HA magnetic beads (Pierce: 88837). Chromatin was adjusted for immunoprecipitation using 1% Triton X-100 and 150mM NaCl then transferred on beads, followed by overnight incubation at 4°C. Immunoprecipitated complexes were washed sequentially with Low Salt Wash Buffer (10 mM Tris-HCl pH 8.0, 1 mM EDTA, 150 mM NaCl, 1% Triton X-100, 0.15% SDS, protease inhibitors), High Salt Wash Buffer (10 mM Tris-HCl pH 8.0, 1 mM EDTA, 500 mM NaCl, Triton X-100, 0.15% SDS, protease inhibitors), LiCl Buffer (10 mM Tris-HCl pH 8.0, 1 mM EDTA, 0.5 mM EGTA, 250 mM LiCl, 1% NP-40, 1% NaDOC, protease inhibitors), and TE buffer. DNA was eluted and purified using QIAGEN columns. ChIP and input DNA were analyzed by qPCR using specific primers. Enrichment was calculated as a percentage of input

or relative to a control region using the ΔΔCt method. Experiments were performed in biological duplicates. Additionally, samples were send for sequencing. Primers used for QPCR are listed below:

Gene/Position	Primer Sequence (5' → 3')
ZDHHC20_pos1_fw	AAAGAAGGTCAAAGAAGGAGAAA
ZDHHC20_pos1_rv	GGCTTAAGTCTATCATTTGCTCT
ZDHHC20_pos2_fw	CCATTCAGCCACTCTATGTCTT
ZDHHC20_pos2_rv	AATGGCAGGAATAAATCCTTACTTATC
MAT1A_fw	GCTAGGAAGAAACTGCATCAAAC
MAT1A_rv	CTCCTCAATACAGCACACTGAT
TXNRD1_fw	AGTGTAACTGTGGAATCTGTATGT
TXNRD1_rv	GCCTACCTGGTGCATTCTT
SELS_1_fw	GATTGAAGAACGGGTGGGA
SELS_1_rv	AATTACTGGTGTGTTCCAGTTTG

Library preparation and sequencing.

DNA concentrations were determined using a Qubit fluorometer (Thermo Fisher Scientific) following the manufacturer's protocol. Chromatin immunoprecipitated DNA was processed using the NEBNext Ultra II DNA Library Prep Kit (New England Biolabs, Version 7.0_9/22) according to the manufacturer's instructions (internal experiment code GFX016). Input DNA amounts varied between 1.5 ng and 5 ng, as specified in the corresponding sample table. Given the absence of initial DNA profile data, a positive control was included during library preparation. Library concentrations were measured using Qubit High Sensitivity (HS) DNA quantification, and fragment size distributions were assessed using a TapeStation TS4200 (Agilent Technologies). All libraries exhibited expected fragment profiles and sufficient yield for sequencing. Prepared libraries were sequenced on the Element Biosciences Aviti platform in a paired-end 150 bp (PE150) run (run ID: AVT0149). Sample-specific identifiers and sequencing metadata are detailed in the supplementary data. Adapter sequences were trimmed using Cutadapt vX.X with TruSeq adapter sequences:

Read 1:AGATCGGAAGAGCACACGTCTGAACTCCAGTCA;

Read2: AGATCGGAAGAGCGTCGTGTAGGGAAAGAGTGT

ChIPseq analysis

To identify and merge significant peaks across multiple conditions, we utilized BEDTools [91](v2.30.0). Initially, overlapping peaks from multiple BED files were merged using the bedtools multiinter function. To ensure a more comprehensive peak detection, an alternative strategy was applied, merging all available BED files in the directory. Following peak merging, signal intensity filtering was performed using deepTools (v3.5.1). The computeMatrix function extracted signal values from bigWig (BW) files over predefined peak regions (Filt_GFP.bed). A threshold of 15 was applied to exclude peaks with excessively high signal intensities. To visualize the signal distribution, a heatmap was generated using plotHeatmap, employing the Oranges_r colormap. Based on the filtered set (sorted_regionsFilt12.bed), another round of peak merging was conducted to ensure that only the most relevant peaks were retained. This final merged peak list contained only peaks present in HEK293T and those retained in K562. To further refine peak selection and exclude aberrant values, we applied an additional filtering step with a stricter intensity threshold (--maxThreshold 150). A final heatmap was generated to visualize the refined peak set. A final heatmap was generated to visualize the refined peak set. Ultimately, the final set of high-confidence peaks used for downstream analysis was stored in sorted_regions_3.bed, representing the most relevant and biologically meaningful peak regions across conditions.

RNAseq

RNA quality was controlled on the TapeStation 4200 (Agilent), which confirmed their integrity. Libraries for mRNA-seq were prepared with the Stranded mRNA Ligation method (Illumina), according to manufacturer's instructions, starting from 800ng RNA. Libraries, all bearing unique dual indexes, were subsequently loaded at 100 pM on a Novaseq 6000 flow cell (Illumina) and sequenced according to manufacturer instructions, yielding pairs of 60 nucleotides reads at a depth of about 70 mio reads pairs per sample. Reads were trimmed of their adapters with bclconvert v00.000.000.3.9.3 (Illumina) and quality-controlled with

fastQC v0.11.9. FastQ Screen v0.14.0 tool was used for screening FASTQ files reads against multiple reference genomes.

RNAseq processing and analysis

Sequencing reads were mapped to the human hg19 genome using hisat2 [D. Kim, B. Langmead, and S. L. Salzberg, "HISAT: a fast spliced aligner with low memory requirements," *Nature Methods*, vol. 12, no. 4, pp. 357–360, Mar. 2015.] with parameters: hisat2 -k 5 --seed 42 --rna-strandness RF. Counts on genes were generated using featureCounts [Y. Liao, G. K. Smyth, and W. Shi, "featureCounts: an efficient general purpose program for assigning sequence reads to genomic features," *Bioinformatics*, vol. 30, no. 7, pp. 923–930, Apr. 2014.]. Only uniquely mapped reads were used for counting on genes. Normalization for sequencing depth was done using the TMM method as implemented in the limma package of Bioconductor [Gentleman et al., 2004]. Differential gene expression analysis was performed using voom (Law et al., 2014) as it has been implemented in the limma package of Bioconductor. A gene was considered to be differentially expressed when the fold change between groups was bigger than 2 and the p-value was smaller than 0.05. A moderated t-test (as implemented in the limma package of R) was used to test significance. P-values were corrected for multiple testing using the Benjamini-Hochberg's method [92]. Gene set enrichment analysis (GSEA) was performed using the ClusterProfiler package in R. The analysis utilized a ranked list of genes and gene set collections downloaded from MsigDB. The GSEA was conducted with the following parameters: the number of permutations was set to 10,000, minimum gene set size was 10, maximum gene set size was 800.

Flow cytometry analysis of membrane permeability and lipid peroxidation

U2OS cells (6 well plate at approximate 1 x 10^6 cells), siRNA depleted as indicated were treated with 5 µM RSL-3 for 24 h. Cells were washed twice in EBSS (10 µM Hepes) and Lipid peroxides stained by Liperfluo (Dojindo) and C11-BODIPY581/591 (Invitrogen). Stock solutions of Liperfluo or BODIPY, prepared in DMSO, according to manufacturer's

instructions were resuspended in EBSS-Hepes to 5 µM (Liperfluo) and 10 µM for Bodipy and used for cell incubation 1 ml per well for 30 min at 37°C. After treatment cells were washed, trypsinized and resuspended in 500 ul EBSS-Hepes. For propidium iodide analysis Liperfluor labelled cells were stained with propidium iodide prior analysis at final concentration 1 µg/ml. Analytical flow cytometry was performed using an LSRII or LSR Fortessa (BD; Becton Dickinson) instrument. For Liperfluor, and BODIPY-oxidated cells were analysed at Excitation: 488 nm, Filter: 530/30; For PI and BODIPY-non-oxidated Excitation:561 nm Filter 610/20. 10,000 events were acquired per each replicate per sample. Results were analyzed using FlowJo.

DSS-induced mice colitis

Six wild-type C57BL/6j mice (8-week-old males) were used. Three (n = 3) mice were used as controls and three mice were given 3% dextran sulfate sodium in the drinking water for 7 days, then switched to regular drinking water for 3 days. Three Control 8-week male were given drinking water that did not contain DSS. During the 10-day experiment, mice were weighted and disease activity index (DAI) was performed daily based on stool consistency, presence of occult blood and body weight loss. On day 10, mice were euthanized with injection of pentobarbital and bled via cardiac puncture, and colon and intestines were collected. For animal experimentation, all procedures were performed according to protocols approved by the Veterinary Authorities of the Canton Vaud and according to the Swiss Law (license VD 3497, EPFL).

Quantification and Statistical Analysis

All experiments were conducted independently a minimum of three times. Unless indicated otherwise, each data point corresponds to a separate experiment yielding consistent outcomes. Statistical evaluations were carried out using Prism software, with graphical representations and detailed statistical information available in the figure legends. For ANOVA, p-values

were calculated using post hoc tests: Tukey's and Sidak's for multiple comparisons between groups, and Dunnett's for comparisons against a control condition. RNA-seq and ChIP-seq analyses were performed using distinct bioinformatics pipelines, as outlined in the Materials and Methods section, to ensure appropriate data handling and statistical evaluation specific to each dataset.

Supplemental information titles and legends

Ontology	setSize	pvalue
GOBP_CHEMICAL_HOMEOSTASIS	772	0.000120555
GOBP_REGULATION_OF_RESPONSE_TO_EXTERNAL_STIMULUS	713	0.000122549
GOCC_VACUOLE	711	0.000122594
GOBP_RESPONSE_TO_LIPID	669	0.000122956
GOBP_DEFENSE_RESPONSE_TO_OTHER_ORGANISM	704	0.000123062
GOBP_RESPONSE_TO_CYTOKINE	698	0.000123183
GOBP_REGULATION_OF_IMMUNE_RESPONSE	599	0.000125423
GOBP_INFLAMMATORY_RESPONSE	550	0.000127146

GOBP_INNATE_IMMUNE_RESPONSE	550	0.000127146
GOBP_CYTOKINE_PRODUCTION	550	0.000127146
GOBP_PROCESS_UTILIZING_AUTOPHAGIC_MECHANISM	510	0.0001287
GOCC_ENDOSOME_MEMBRANE	479	0.000129433
GOBP_REGULATION_OF_DEFENSE_RESPONSE	464	0.000129836
GOCC_VACUOLAR_MEMBRANE	417	0.000131752
GOBP_RESPONSE_TO_BACTERIUM	422	0.000131961

Table S2. Gene Set Enrichment Analysis-GSEA dot plot of ZNF354A upregulated enriched GO-terms depicted in Fig 3C.

Table S3. Fold Enrichment of Selected Anti-Oxidant genes up-regulated upon siZNF354A. Fold enrichment and adjusted P values are indicated.

symbol	genename	Fold_Change_siZNF354A	P value (adj)
HMOX1	heme oxygenase 1	40.15	5.17E-20
ATF3	activating transcription factor 3	37.77	5.52E-19
CYP19A1	cytochrome P450 family 19 subfamily A member 1	18.88	4.95E-07
MAT1A	methionine adenosyltransferase 1A	13.26	4.49E-10
NMRAL2P	NmrA like redox sensor 2, pseudogene	10.28	3.79E-16
SOD2	superoxide dismutase 2	9.69	7.70E-19
NDUFA9P1	NADH:ubiquinone oxidoreductase subunit A9 pseudogene 1	7.90	0.007637324
SLC6A13	solute carrier family 6 member 13	5.38	2.80E-05
ABCC2	ATP binding cassette subfamily C member 2	5.37	1.60E-10
SQSTM1	sequestosome 1	5.21	2.20E-22
UGT1A1	UDP glucuronosyltransferase family 1 member A1	5.09	0.021483943
TSTD1	thiosulfate sulfurtransferase like domain containing 1	4.98	0.020989411
SLC2A9	solute carrier family 2 member 9	4.90	0.023995657
FGF13	fibroblast growth factor 13	4.37	0.035094442
SLC6A15	solute carrier family 6 member 15	4.11	3.76E-17
MAFF	MAF bZIP transcription factor F	4.01	7.21E-17
SLC5A11	solute carrier family 5 member 11	3.96	0.039618067
CES3	carboxylesterase 3	3.65	0.000488213
SLC7A11	solute carrier family 7 member 11	3.59	5.49E-19
GGT1	gamma-glutamyltransferase 1	3.35	2.80E-06
FTH1	ferritin heavy chain 1	3.21	8.59E-22
NDUFAB1P1	NADH:ubiquinone oxidoreductase subunit AB1 pseudogene 1	3.20	0.156910949
NDUFA3P4	NADH:ubiquinone oxidoreductase subunit A3 pseudogene 4	3.09	0.072081463
SLC2A3	solute carrier family 2 member 3	2.76	1.33E-15
HMGCS1	3-hydroxy-3-methylglutaryl-CoA synthase 1	2.73	1.27E-17
GCLC	glutamate-cysteine ligase catalytic subunit	2.70	1.32E-16
CTH	cystathionine gamma-lyase	2.49	7.59E-12
HSD17B14	hydroxysteroid 17-beta dehydrogenase 14	2.48	4.98E-15
FTL	ferritin light chain	2.46	1.82E-19
EGR1	early growth response 1	2.43	1.87E-12
P4HA2	prolyl 4-hydroxylase subunit alpha 2	2.43	2.22E-16
SLC6A6	solute carrier family 6 member 6	2.41	3.97E-17
SLC3A2	solute carrier family 3 member 2	2.24	5.43E-18
MGST1	microsomal glutathione S-transferase 1	2.23	1.22E-18
GSTO2	glutathione S-transferase omega 2	2.18	4.76E-11
NDUFA7	NADH:ubiquinone oxidoreductase subunit A7	2.12	8.05E-05
GCLM	glutamate-cysteine ligase modifier subunit	2.07	4.35E-16

SRXN1	sulfiredoxin 1	2.05	1.40E-10
PPT1	palmitoyl-protein thioesterase 1	2.00	4.07E-16
BLVRB	biliverdin reductase B	1.98	7.61E-14
GLRX	glutaredoxin	1.96	2.62E-14
NDUFV2	NADH:ubiquinone oxidoreductase core subunit V2	1.93	3.52E-05
MSMO1	methylsterol monooxygenase 1	1.88	3.65E-16
HMGCR	3-hydroxy-3-methylglutaryl-CoA reductase	1.87	1.59E-15
HSD17B2	hydroxysteroid 17-beta dehydrogenase 2	1.85	3.64E-06
TXN	thioredoxin	1.79	4.45E-17
SLC2A6	solute carrier family 2 member 6	1.77	7.37E-10
HSD11B1L	hydroxysteroid 11-beta dehydrogenase 1 like	1.77	2.35E-09
FSP1/AIFM2	apoptosis inducing factor mitochondria associated 2	1.73	5.60E-14
PTGR1	prostaglandin reductase 1	1.72	6.90E-15
LSS	lanosterol synthase	1.68	5.04E-15
ABCC3	ATP binding cassette subfamily C member 3	1.67	1.16E-10
MAFG	MAF bZIP transcription factor G	1.66	1.27E-13
UGT2B7	UDP glucuronosyltransferase family 2 member B7	1.64	0.568204859
TXNRD1	thioredoxin reductase 1	1.64	6.17E-16
FDXR	ferredoxin reductase	1.64	1.14E-12
DHCR7	7-dehydrocholesterol reductase	1.61	2.87E-12
GCH1	GTP cyclohydrolase 1	1.61	2.41E-06
CES2	carboxylesterase 2	1.57	9.80E-13
SLC6A4	solute carrier family 6 member 4	1.56	0.536914663
SOD3	superoxide dismutase 3	1.53	1.51E-07
GPX3	glutathione peroxidase 3	1.53	3.00E-10
SLC6A17	solute carrier family 6 member 17	1.52	1.54E-10
SLC2A13	solute carrier family 2 member 13	1.52	0.000187486
GSTO1	glutathione S-transferase omega 1	1.51	4.37E-13
HSD17B7	hydroxysteroid 17-beta dehydrogenase 7	1.51	1.27E-07
SLC39A6	solute carrier family 39 member 6	1.51	9.96E-13
SC5D	sterol-C5-desaturase	1.50	1.51E-12
SLC39A14	solute carrier family 39 member 14	1.50	3.23E-13
SLC2A5	solute carrier family 2 member 5	1.49	0.071681887
HSPA1A	heat shock protein family A (Hsp70) member 1A	1.49	2.22E-09
HSD17B3	hydroxysteroid 17-beta dehydrogenase 3	1.49	0.47555887
NSDHL	NAD(P) dependent steroid dehydrogenase-like	1.46	2.31E-10
P4HA1	prolyl 4-hydroxylase subunit alpha 1	1.45	3.20E-11
GSR	glutathione-disulfide reductase	1.45	4.01E-12
GLRX3	glutaredoxin 3	1.45	7.10E-13
HSD17B12	hydroxysteroid 17-beta dehydrogenase 12	1.43	2.18E-12
ME1	malic enzyme 1	1.43	3.58E-12

ATF7	activating transcription factor 7	1.39	4.25E-10
HSD17B7P2	hydroxysteroid 17-beta dehydrogenase 7 pseudogene 2	1.37	0.013983432
SELENOF	selenoprotein F	1.36	3.64E-11
SQLE	squalene epoxidase	1.35	2.41E-10
SELENOS	selenoprotein S	1.35	1.39E-09
MGST3	microsomal glutathione S-transferase 3	1.35	4.89E-10
SLC5A6	solute carrier family 5 member 6	1.34	5.70E-09
NDUFAF4	NADH:ubiquinone oxidoreductase complex assembly factor 4	1.33	1.84E-07
ATF4	activating transcription factor 4	1.32	2.50E-09
SEPHS2	selenophosphate synthetase 2	1.32	1.34E-09
HBEGF	heparin binding EGF like growth factor	1.32	3.69E-09
NFE2L2	NFE2 like bZIP transcription factor 2	1.31	1.25E-10
SLC39A13	solute carrier family 39 member 13	1.31	2.27E-10
PRDX4	peroxiredoxin 4	1.31	3.66E-10
ABCC5	ATP binding cassette subfamily C member 5	1.30	3.65E-09
TXNL4B	thioredoxin like 4B	1.29	3.12E-06
AGER	advanced glycosylation end-product specific receptor	1.28	0.00846785
FDFT1	farnesyl-diphosphate farnesyltransferase 1	1.27	1.73E-09
A1BG-AS1	A1BG antisense RNA 1	1.27	0.000132829
HSD17B10	hydroxysteroid 17-beta dehydrogenase 10	1.26	3.49E-08
SLC39A5	solute carrier family 39 member 5	1.25	0.771225403
NDUFAF7	NADH:ubiquinone oxidoreductase complex assembly factor 7	1.24	4.09E-05
RXRA	retinoid X receptor alpha	1.22	3.17E-08
PRDX1	peroxiredoxin 1	1.22	2.34E-09
PRDX5	peroxiredoxin 5	1.21	2.47E-08
NDUFAF2	NADH:ubiquinone oxidoreductase complex assembly factor 2	1.20	2.76E-05
PRDX6-AS1	PRDX6 antisense RNA 1	1.20	0.204747522
NRG1	neuregulin 1	1.19	8.97E-06
PGD	phosphogluconate dehydrogenase	1.19	1.98E-08
GSTM3	glutathione S-transferase mu 3	1.18	2.79E-05
SELENOM	selenoprotein M	1.18	0.000374032
NQO1	NAD(P)H quinone dehydrogenase 1	1.18	3.96E-07
GPX4	glutathione peroxidase 4	1.17	2.59E-06
SLC6A8	solute carrier family 6 member 8	1.17	9.44E-07
TXNL1	thioredoxin like 1	1.16	9.03E-07
NDUFA9	NADH:ubiquinone oxidoreductase subunit A9	1.16	0.001172969
TXNDC11	thioredoxin domain containing 11	1.15	2.33E-05
NDUFS4	NADH:ubiquinone oxidoreductase subunit S4	1.14	0.000490

			966
NDUFS7	NADH:ubiquinone oxidoreductase core subunit S7	1.14	0.000190645
NDUFB9	NADH:ubiquinone oxidoreductase subunit B9	1.13	2.85E-05
NDUFA5	NADH:ubiquinone oxidoreductase subunit A5	1.13	2.73E-05
NDUFA13	NADH:ubiquinone oxidoreductase subunit A13	1.13	0.066403273
SELENOW	selenoprotein W	1.13	0.001378797
SLC39A11	solute carrier family 39 member 11	1.12	0.008982893
SLC2A1	solute carrier family 2 member 1	1.12	8.47E-06
TGFBR2	transforming growth factor beta receptor 2	1.12	2.16E-05
SLC39A1	solute carrier family 39 member 1	1.12	6.02E-05
NDUFA3	NADH:ubiquinone oxidoreductase subunit A3	1.11	0.001680968
SLC39A9	solute carrier family 39 member 9	1.11	0.000112706
G6PD	glucose-6-phosphate dehydrogenase	1.11	4.54E-05
HSD17B4	hydroxysteroid 17-beta dehydrogenase 4	1.11	0.000170067
NDUFB4	NADH:ubiquinone oxidoreductase subunit B4	1.11	0.00041982
TXNRD2	thioredoxin reductase 2	1.11	0.003767673
TXNDC5	thioredoxin domain containing 5	1.11	0.02040294
KEAP1	kelch like ECH associated protein 1	1.09	0.005236277
NDUFB2	NADH:ubiquinone oxidoreductase subunit B2	1.09	0.006186759
CBR1	carbonyl reductase 1	1.09	0.000529278
HSD3B7	hydroxy-delta-5-steroid dehydrogenase, 3 beta- and steroid delta-isomerase 7	1.09	0.104223992
SLC39A7	solute carrier family 39 member 7	1.08	0.000568412
SLC39A3	solute carrier family 39 member 3	1.08	0.033023583
NDUFB11	NADH:ubiquinone oxidoreductase subunit B11	1.08	0.007131916
NDUFB8	NADH:ubiquinone oxidoreductase subunit B8	1.08	0.030151898
ATF7IP	activating transcription factor 7 interacting protein	1.08	0.013291938
NDUFA4	NDUFA4 mitochondrial complex associated	1.08	0.007472587
SLC5A12	solute carrier family 5 member 12	1.08	0.916781829
NDUFB2-AS1	NDUFB2 antisense RNA 1	1.08	0.557493874
SELENOK	selenoprotein K	1.07	0.041589256
NDUFAF1	NADH:ubiquinone oxidoreductase complex assembly factor 1	1.07	0.040454658
GLRX2	glutaredoxin 2	1.07	0.077775603

NDUFS3	NADH:ubiquinone oxidoreductase core subunit S3	1.07	0.017784465
NDUFA2	NADH:ubiquinone oxidoreductase subunit A2	1.06	0.087243133
ATF2	activating transcription factor 2	1.06	0.033946411
NDUFAF8	NADH:ubiquinone oxidoreductase complex assembly factor 8	1.06	0.178985006
NDUFV2-AS1	NDUFV2 antisense RNA 1	1.06	0.7589391
NDUFA1	NADH:ubiquinone oxidoreductase subunit A1	1.06	0.073019188
HSP90AB1	heat shock protein 90 alpha family class B member 1	1.05	0.002553646
NDUFS2	NADH:ubiquinone oxidoreductase core subunit S2	1.05	0.052296262
TXNDC15	thioredoxin domain containing 15	1.04	0.088051517
SELENOH	selenoprotein H	1.04	0.1656338
NDUFS8	NADH:ubiquinone oxidoreductase core subunit S8	1.03	0.252041917
DNAJB1	DnaJ heat shock protein family (Hsp40) member B1	1.03	0.213084381
TXNL4A	thioredoxin like 4A	1.03	0.354570706
TXN2	thioredoxin 2	1.02	0.392686822
NDUFAF5	NADH:ubiquinone oxidoreductase complex assembly factor 5	1.02	0.609175291
TGFA	transforming growth factor alpha	1.02	0.835135275
NDUFB4P12	NADH:ubiquinone oxidoreductase subunit B4 pseudogene 12	1.01	0.977012913
SLC2A12	solute carrier family 2 member 12	1.01	0.796322247
SELENOI	selenoprotein I	1.01	0.82542347
SLC6A16	solute carrier family 6 member 16	1.01	0.974317842
NDUFS1	NADH:ubiquinone oxidoreductase core subunit S1	1.00	0.841574944
NDUFB5	NADH:ubiquinone oxidoreductase subunit B5	1.00	0.944752474